Combustion and Flame 163 (2016) 284–300

Contents lists available at ScienceDirect

Combustion and Flame

journal homepage: www.elsevier.com/locate/combustflame

Transient combustion of a methane-hydrate sphere

Tali Bar-Kohany [a,b,*], William A. Sirignano [a]

[a] Department of Mechanical and Aerospace Engineering, University of California, Irvine, CA 92697-3975, United States
[b] Department of Mechanical Engineering, Ben-Gurion University of the Negev, Beer-Sheva, Israel

ARTICLE INFO

Article history:
Received 30 May 2015
Revised 1 October 2015
Accepted 2 October 2015
Available online 2 November 2015

Keywords:
Methane-hydrate
Moving boundaries
Transient evaporation
Quasi-steady combustion

ABSTRACT

A solution is presented for the spherically symmetric, transient vaporization and combustion of methane-hydrate in a three-phase configuration with rate control by liquid-phase diffusion. The simulation has two moving boundaries due to a solid methane-hydrate core that melts, a transient water shell with small methane gas bubbles, and a quasi-steady gas phase with Stefan convection and advection, diffusion, and chemical reaction. First, a model for melting and vaporization without oxidation is considered. Then, the combustion process is considered at an infinite chemical reaction rate (i.e., a "thin flame" case).

The characteristics of the methane-hydrate combustion are examined at different ambient temperatures, pressures and compositions and values of methane-to-water mass ratio. Different values of products in the environment are examined, considering individual particles burning in an environment which has been heated by the presence of other burning droplets, as in-situ production methods are currently developed. An appropriate characteristic time scaling is identified for particles of initial radius of 100 μm or less, considering these will be relevant for combustion of grounded hydrates.

1. Introduction

Methane-hydrates are ice-like crystalline solids, consisting of a non-stoichiometric compounds of water cavities and methane gas molecules [1]. At high pressures and low temperatures, methane fills cavities within the ice preventing hydrogen-bond strain and breakage. At zero centigrade, hydrate ice, methane gas and liquid water can co-exist below 300 m in the ocean (Fig. 1) and under 200 m in the permafrosts.

The interest in high pressure burning is generated by three factors: greater thermal efficiency for power applications, greater stability of the hydrate, and opportunity for in situ combustion. High pressures means, for example, higher values of availability, namely higher thermodynamic potential that lead to improved thermal efficiency for power delivery.

In-situ production of hydrocarbons is conducted at the Messoyakha gas field in the northern part of the west Siberian Basin for several decades. Extraction of gas from the gas-hydrate layer by depressurization may be hampered by the formation of ice or reformation of gas-hydrates due to the endothermic nature of the hydrate dissociation process [3]. In-situ production possess potential advantages since it is likely to avoid part of the handling and transportation losses, identified by Demirbas [4] as one of the key problem in the production of methane from the hydrate layer. In-situ combustion has the potential to avoid that problem. In-situ production methods are currently developed. For example, Cranganu [5] and Pfefferle [6] suggest to provide the energy that is required for the gas-hydrate dissociation by burning small amount of gas extracted by from the hydrates within a borehole drilled to the depth at which hydrates prevail.

Due to its relatively small molecule size (~0.4 nm), methane-hydrate forms a cubic structure [7]. Experimental evidence of gas-hydrates burning has been demonstrated over the recent years [8,9].

Methane, being the major component of many natural gas sources, has been the focus of a growing interest during the past decades. This trend is expected to grow even further in the future. For example, U.S. total natural gas consumption grows from 690 million cubic meters in 2011 to 835 million cubic meters in 2040 in the AEO2013 Reference case ([10, Fig. 85]). Most of the increase in natural gas consumption is predicted to result from an increase in shale gas extraction. Natural gas production from shale gas includes linking laminates that store free gas by a hydraulic fracture (fracking) [11]. However, hydraulic fracturing may pose some environmental and health risks such as methane leakage into drinking water reservoirs [12]. Methane hydrates are found in sediment at the edge of the continental shelves.[1] Thus, exploiting methane hydrates as an energy source is appealing.

* Corresponding author. Fax: +972 86472813.
E-mail addresses: kahany@post.bgu.ac.il, talibar1@gmail.com (T. Bar-Kohany), sirignan@uci.edu (W.A. Sirignano).

[1] http://woodshole.er.usgs.gov/project-pages/hydrates/climate.html.

http://dx.doi.org/10.1016/j.combustflame.2015.10.004
0010-2180/

Nomenclature

latin letters

b	water-to-fuel mole ratio for hydrate
C_i	Shvab–Zel'dovich constants
C_p	constant pressure specific heat
D	diffusion coefficient
E_A	activation energy
F	shape factor
h	specific thermal enthalpy
K_1	evaporation rate
K_2	droplet-to-solid core radii ratio
L	latent heat of vaporization
m	stoichiometric mass ratio
$\dot{m}$	mass flow rate
M	molecular weight
p	pressure
$\dot{q}$	conductive heat flux
Q	heat of combustion
r	radial coordinate
R	particle radius
R_u	universal gas constant
t	time
T	temperature
u	velocity
Y	mass fraction
Z	$= 1/(4\pi\rho D)$, assumed to be a constant for the gas

Greek letters

α	thermal diffusivity
β	Shvab–Zel'dovich function
ϵ	emissivity
η	normalized radial coordinate
λ	thermal conductivity
ν	stoichiometric constant, mass-based
$\bar{\nu}$	stoichiometric constant, mole-based
ρ	density
σ_B	Stefan–Boltzmann constant
τ	normalized time
$\dot{\omega}$	chemical reaction rate

Subscripts

∞	ambient value
BM	bubbly mixture
BM, s	bubbly mixture–gas interface, on bubbly mixture side
f	formation, or flame
F	fuel
g	gas phase
i	the ith species
L	liquid phase
m	surface value at melting front
$melt$	melting
mix	mixture
MH	methane-hydrate
s	surface value, on gas side of interface
vap	vaporization
0	initial

Superscript

o	reference value

In order to increase burning rates, solid fuels are commonly injected into a combustor in a pulverized form. Burning at high pressures is more efficient when power is to be delivered; it also would be necessary for in-situ combustion. Thus, we focus on small hydrate particles burning at high pressures.

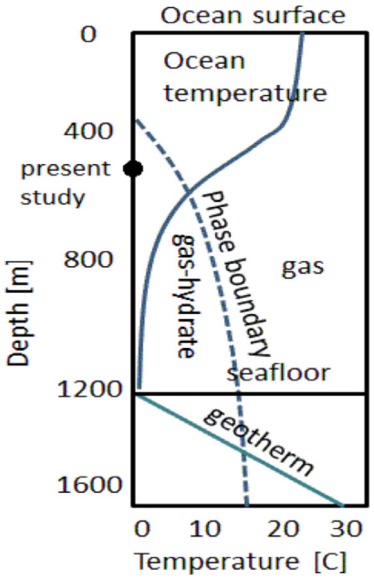

Fig. 1. Gas hydrate phase diagram; reconstructed following Ref. [2].

This study presents a solution to a spherically symmetric combustion process of a three-phase particle. A single, isolated particle is an ideal representation of the physical processes that the particle undergoes in a dilute region of a spray or any bulk. Certainly, the model of the isolated, spherically symmetric fuel droplet has outlived its usefulness for traditional fuels where the practical consideration has dense sprays moving relative to the oxidizing environment. However, in this new venture concerning the combustion of hydrate particles, the treatment of an isolated, spherically symmetric (i.e., stagnant) particle can be justified.

High water content is an issue in the modeling but not a blockage to theoretical development. Chemical equilibrium calculations show that oxidation of the methane can occur with high water content. Also, drainage of some of the water before vaporization is a possible technical solution. This cannot be represented in our spherically symmetric configuration but can be described in later multidimensional configurations and has been seen in the lab.

Certainly, one should eventually examine a cloud of particles but surely that is not the first configuration to be studied. Based on our extensive experience with burning sprays and droplets, it can be assumed that the cloud will cause (sometimes large) perturbations to the behavior of the individual particle. However, the individual isolated particle should be a wonderful building block.

Assuming conduction prevails within the droplet leads to a spherically symmetric configuration. Sirignano [13], Sazhin [14], Law [15] and others have demonstrated that the spherically symmetric configuration consolidates fundamental physical processes, such as transient heat transfer, mass diffusion and phase equilibrium, that remain valid even when the flow become complex [16]. The spherically symmetric configuration allows the diffusion of the vaporized species outwards, while the oxidizer diffuses inwards, towards the droplet surface. Stefan convection accounts for the regression of the boundaries of the droplet during the vaporization and combustion processes. In the present study, two such boundaries exist, the outer boundary at the liquid-gas interface and the inner boundary at the liquid–solid interface. The heat that is conducted into the particle is balanced by the vaporization process at the liquid-gas interface, the melting process at the liquid-solid interface, and the heating of the liquid.

2. Problem formulation

A cold, solid, spherical methane-hydrate core is placed in a hot, quiescent, air environment, at a constant pressure and temperature.

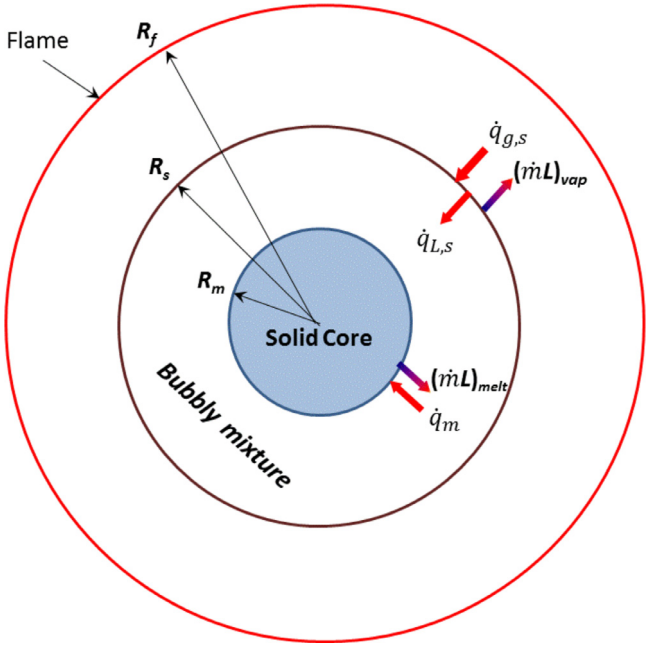

Fig. 2. Hydrate particle. The radii are not depicted here in proper proportion.

Due to the high temperature, the solid core begins to melt and a mixture comprised of the molten liquid and the methane gas bubbles is formed around the core (Fig. 2).

Hydrates are formulated at high pressures, i.e. hundreds of atmospheres. Thus, when placed in a considerably lower pressure environment, the hydrate cavities, in which the methane is caged, may be considered as thermodynamically unstable. Nonetheless, methane-hydrates introduced at low pressures and isothermal conditions destabilizes immediately the sample. Experiments show that a thermal regime exists where methane hydrate meta-stably preserves in bulk [17]. Those authors refer to an anomalous preservation region, and report that samples that were depressurized to 1 atm at temperatures between 245 K and 272 K never attained 50% dissociation and samples between 242 K and 271 K preserved 93% of the hydrate for at least 24 h. Nonetheless, though samples remained stable up to 24 h at lower pressures, the volume ratio at low pressures between the methane, once escaped the matrix, and the liquid water will be very large.

The following assumptions were employed in the analysis. The temperature of the hydrate core is low enough so that the typical dissociation time greatly exceeds that of the melting and evaporation times. In the present study the pressure is 50 atm and the core temperature remains at the melting temperature. It is reasonable to assume that heterogeneous de-crystallization with preferred sites at the solid-liquid interface prevails over homogeneous de-crystallization through the interior. Thus, the melting rate is determined by the rate of heat transfer to the interface. The droplet remains spherical throughout the evaporation and combustion processes. For initial particle radius in the range of 100 μm to 1 mm, surface tension forces overpower inertia and gravitational forces. Buoyancy effects are assumed to be negligible, as compared to inertial or viscous forces, for particles in this size range. Dripping or drainage of the melted ice is also neglected although its impact on quantitative results can be significant; the water remains in a film around the solid ice core until it vaporizes. Thus, only Stefan convection is considered. Dufour and Soret diffusion effects are negligible. A Fickian diffusion is assumed with a unity Lewis number. Thermal radiation is negligible as compared with heat conduction at low ambient temperatures. However, if considering the particles as burning in the presence of other particles, i.e., in a spray form, for example, the ambient temperatures may not allow the neglect of radiation. For small spheres (~100 μm), radiation can be neglected. Thermodynamic equilibrium of the water at the liquid-vapor interface prevails. Composition of the hydrate particle is maintained throughout the processes, due to low Henry constants (20–30 ppm at the relevant temperatures, [18,19]). Thus, at high pressure, the methane exists in small bubbles through the liquid shell and does not dissolve in it to any significant extent. The gaseous species, apart from the methane itself, are assumed not to dissolve into the liquid shell. Of course, as the thermodynamic critical point is approached, more gases, including methane, product gases, and ambient gases, would dissolve in the water. However, the critical pressure of water is above 200 atm.

Heat transfer within the bubbly mixture is slower than through the gas phase; therefore, the heat transfer within the gas phase is considered to be a quasi-steady process. Consistent with the quasi-steady assumption, only the established flame case is studied here without attention to ignition. The product of the density and diffusion coefficient ρD is constant.

We solve the global continuity, species continuity, and energy equations for all three phases simultaneously.

2.1. Gas phase

The continuity equation for the quasi-steady gas phase is simply

$$\dot{m} = 4\pi\rho u r^2 \tag{1}$$

The species equation for a quasi-steady process, after incorporating the continuity equation, becomes

$$\rho D\frac{d}{dr}\left(r^2\frac{dY_i}{dr}\right) - \rho u r^2\frac{dY_i}{dr} = -\rho r^2\dot{w}_i \tag{2}$$

where $\dot{w}_F < 0$

For a stoichiometric reaction of methane, the chemical balance of the different species is

$$CH_4 + \bar{\nu}(O_2 + 3.76N_2) \longrightarrow CO_2 + \bar{\nu}\,H_2O + 3.76\bar{\nu}\,N_2 \tag{3}$$

where $\bar{\nu} \equiv n_{O_2}/n_F = 2$

The volumetric, one-step, chemical reaction rate is defined as $\dot{w}_F$. The chemical reaction rates of the other species are determined according to their mass ratios:

$$\dot{w}_{O_2} = \frac{1}{\nu}\dot{w}_F, \quad \dot{w}_{H_2O} = -\nu_3\dot{w}_F, \quad \dot{w}_{CO_2} = -\nu_4\dot{w}_F \tag{4}$$

where

$$\nu = \frac{M_F/M_{O_2}}{\bar{\nu}} = 0.251, \quad \nu_3 \equiv \frac{m_{H_2O}}{m_F} = 2.246,$$
$$\nu_4 \equiv \frac{m_{CO_2}}{m_F} = 2.2743 \tag{5}$$

The energy equation, after neglect of work or kinetic energy since the medium has low speed and, assuming $Le = 1$, is similar to the species equation:

$$\rho D\frac{d}{dr}\left(r^2\frac{dh}{dr}\right) - \rho u r^2\frac{dh}{dr} = -\rho r^2\Sigma_i Q_i\dot{w}_i,$$

or, for constant specific heat and one-step reaction,

$$\frac{\dot{m}}{4\pi}C_{p,g}\frac{d}{dr}\left(\frac{r^2}{\dot{m}Z}\frac{d(T_g - T_\infty)}{dr} - (T_g - T_\infty)\right) = -\rho r^2 Q_F\dot{w}_F \tag{6}$$

where $Z \equiv C_{p,g}/(4\pi\lambda_g) = 1/(4\pi\rho D)$, and Q is the heat of combustion

$$Q_F \equiv h^0_{f,F} - \left(\nu_3 h^0_{f,H_2O} + \nu_4 h^0_{f,CO_2}\right) \tag{7}$$

With the similarity of the species (Eq. (2)) and energy (Eq. (6)) equations, it is convenient to present the solution in the form of

Shvab–Zel'dovich (S–Z) functions. We have four species in the reaction plus enthalpy; therefore, we use four functions, which are defined as follows:

$$\begin{aligned}\beta_1 &\equiv Y_F - \nu(Y_{O_2} - Y_{O_2,\infty})\\ \beta_2 &\equiv Y_F + \frac{C_{p,g}(T_g - T_\infty)}{Q_F}\\ \beta_3 &\equiv (Y_{H_2O} - Y_{H_2O,\infty}) + \nu\nu_3(Y_{O_2} - Y_{O_2,\infty})\\ \beta_4 &\equiv (Y_{CO_2} - Y_{CO_2,\infty}) + \nu\nu_4(Y_{O_2} - Y_{O_2,\infty})\end{aligned} \tag{8}$$

With these definitions, both the species and energy equations become homogeneous equations, as the non-homogeneous, RHS of these equations is zeroed.

The solutions are found in the form of

$$\beta_i = C_{i1} + C_{i2}\exp\left(-\frac{\dot{m}_g Z}{r}\right) \tag{9}$$

At infinity $\beta_{i,\infty} = 0$, and hence $C_{i1} = -C_{i2}$. Considering the general solution for the S–Z function (9), we obtain

$$C_{i2} = \frac{\beta_{i,s}}{\exp\left(-\frac{\dot{m}_g Z}{R_s}\right) - 1} \tag{10}$$

Thus,

$$\beta_i = \beta_{i,s}\frac{\exp\left(-\frac{\dot{m}_g Z}{r}\right) - 1}{\exp\left(-\frac{\dot{m}_g Z}{R_s}\right) - 1} \tag{11}$$

where

$$\begin{aligned}\beta_{1,s} &= Y_{F,s} - \nu(Y_{O_2,s} - Y_{O_2,\infty})\\ \beta_{2,s} &= Y_{F,s} + \frac{C_{p,g}(T_s - T_\infty)}{Q_F}\\ \beta_{3,s} &= (Y_{H_2O,s} - Y_{H_2O,\infty}) + \nu\nu_3(Y_{O_2,s} - Y_{O_2,\infty})\\ \beta_{4,s} &= (Y_{CO_2,s} - Y_{CO_2,\infty}) + \nu\nu_4(Y_{O_2,s} - Y_{O_2,\infty})\end{aligned} \tag{12}$$

The boundary conditions for the five variables at infinity are known ($Y_{F,\infty}, Y_{H_2O,\infty}, Y_{CO_2,\infty}, Y_{O_2,\infty}, T_\infty,$).

Let us determine the S–Z functions, as we will use them later in the analysis.

$$\frac{d\beta_i}{dr} = \frac{\dot{m}_g Z}{r^2}\beta_{i,s}\frac{\exp\left(-\frac{\dot{m}_g Z}{r}\right)}{\exp\left(-\frac{\dot{m}_g Z}{R_s}\right) - 1} \tag{13}$$

At the surface,

$$\frac{d\beta_i}{dr})_s = \frac{\dot{m}_g Z}{R_s^2}\beta_{i,s}\frac{\exp\left(-\frac{\dot{m}_g Z}{R_s}\right)}{\exp\left(-\frac{\dot{m}_g Z}{R_s}\right) - 1} = \frac{\dot{m}_g Z}{R_s^2}\beta_{i,s}\frac{1}{1 - \exp\left(+\frac{\dot{m}_g Z}{R_s}\right)} \tag{14}$$

For thin flame conditions, the oxygen is fully consumed at the flame, thereby its value at the surface, as well as its derivative, is zero. $Y_{O_2,s} = \frac{dY_{O2}}{dr})_s = 0$, thus

$$\begin{aligned}\frac{d\beta_1}{dr})_s &= \frac{dY_F}{dr})_s\\ \frac{d\beta_2}{dr})_s &= \frac{dY_F}{dr})_s + \frac{C_{p,g}}{Q_F}\frac{dT_g}{dr})_s\\ \frac{d\beta_3}{dr})_s &= \frac{dY_{H_2O}}{dr})_s\\ \frac{d\beta_4}{dr})_s &= \frac{dY_{CO_2}}{dr})_s\end{aligned} \tag{15}$$

For example,

$$\frac{d\beta_1}{dr})_{s,TF} = \frac{dY_F}{dr})_s = (Y_{F,s} + \nu Y_{O_2,\infty})\frac{\dot{m}_g Z}{R_s^2}\frac{E_s}{E_s - 1} \tag{16}$$

where $E_s \equiv \exp\left(-\frac{\dot{m}_g Z}{R_s}\right)$

Flame radius: At the (thin) flame, both the fuel and the oxygen are zeroed. This assumption determines the flame location.

$$\begin{aligned}\alpha_1(R_f) &= \nu Y_{O_2,\infty} = (Y_{F,s} + \nu Y_{O_2,\infty})\frac{\exp\left(-\frac{\dot{m}_g Z}{R_f}\right) - 1}{\exp\left(-\frac{\dot{m}_g Z}{R_s}\right) - 1}\\ \nu Y_{O_2,\infty}(E_s - 1) &= (Y_{F,s} + \nu Y_{O_2,\infty})(E_f - 1)\\ \exp\left(-\frac{\dot{m}_g Z}{R_f}\right) &= 1 + \frac{\nu Y_{O_2,\infty}}{Y_{F,s} + \nu Y_{O_2,\infty}}(E_s - 1)\\ -\frac{\dot{m}_g Z}{R_f} &= \ln\left(\frac{Y_{F,s} + \nu Y_{O_2,\infty}E_s}{Y_{F,s} + \nu Y_{O_2,\infty}}\right)\\ R_f &= -(\dot{m}_g Z)/\ln\left(\frac{Y_{F,s} + \nu Y_{O_2,\infty}E_s}{Y_{F,s} + \nu Y_{O_2,\infty}}\right)\end{aligned} \tag{17}$$

2.2. Outer interface: gas phase–bubbly mixture ("s")

The mass fraction of the water at the bubbly mixture–gas interface from the gaseous side is resolved by mass weighting of the local, single-phase water vapor mass fraction and the fuel mass fraction over the surface of the liquid–gas interface.

$$Y_{H_2O,s} = Y_{H_2O,s,local}\frac{bM_{H_2O}}{bM_{H_2O} + M_F} \tag{18}$$

The local water mass fraction ($Y_{H_2O,s,local}$) is calculated by the ratio of the water vapor-to-total densities at phase equilibrium for a situation without methane. The water vapor density (ρ_v) is determined by the total pressure and surface temperature (taken from NIST tables,[2] see selected thermophysical properties in the Appendix).

$$Y_{H_2O,s,local} = \frac{\rho_v}{\rho_s} \tag{19}$$

The total density may be evaluated by the ideal gas law. This implies that the water mass fraction at the droplet surface is an implicit function.

$$\rho_s = \frac{p M_{Mix,s}}{R_u T_s} \tag{20}$$

$$M_{Mix,s} = \left(\Sigma_j \frac{Y_{s,j}}{M_j}\right)^{-1} \tag{21}$$

2.2.1. Mass balances

At the liquid–gas interface, the conservation equations serve as boundary conditions for the species. The fuel mass balance at the surface is [20, p. 61]

$$\dot{m}_{F,BM,s} = \dot{m}_{F,g,s} - 4\pi(\rho D)R_s^2\frac{\partial Y_F}{\partial r})_s \tag{22}$$

where $\dot{m}_{BM}$ is the bubbly mixture mass flux relative to the laboratory frame.

Assuming uniform density throughout the bubbly mixture ($\rho_{BM} = \rho_{BM,s} = f(t)$) then it is a function of time only

$$\dot{m}_{BM} = 4\pi r^2 \rho_{BM} u_{BM} = f(t) \tag{23}$$

[2] http://webbook.nist.gov/chemistry/fluid/.

$$\rho_{BM} = \frac{m_{H_2O} + m_F}{V_{H_2O} + V_F} = m(Y_{H_2O} + Y_F)/\left(\frac{m_{H_2O}}{\rho_{H_2O}} + \frac{m_F}{\rho_F}\right)$$

$$\rho_{BM} = \left(\frac{Y_{H_2O}}{\rho_{H2O}} + \frac{Y_F}{\rho_F(P, \overline{T_{BM}})}\right)^{-1} = f(t) \tag{24}$$

where $\overline{T_{BM}} = (T_{melt} + T_s)/2$.

$$\rho_F = \frac{pM_F}{R_u \overline{T_{BM}}} \tag{25}$$

The fuel mass flux escaping across the moving interface is proportional to the total mass flux relative to the droplet surface, with $Y_{F,BM}$ as the proportionality constant. Assuming the fuel mass fraction across the bubbly mixture is uniform, it is determined by its value within the icy core $Y_{F,BM} = Y_{F,MH}$.

$$\dot{m}_{F,BM,rel} = \dot{m}_{F,BM,s} = Y_{F,BM}\dot{m}_{vap}$$

$$\dot{m}_{F,BM,s} = Y_{F,BM,s}\, 4\pi R_s^2\, \rho_{BM}\left(u_{BM,s} - \frac{dR}{dt})_s\right) \tag{26}$$

Substituting Eq. (26) and the fuel mass fraction gradient at the surface (Eq. (16)) into the fuel mass balance at the outer surface (Eq. (22)) enables evaluation of the fuel mass fraction at the outer surface

$$Y_{F,BM,s}\, 4\pi R_s^2\, \rho_{BM}\left(u_{BM,s} - \frac{dR}{dt})_s\right) = Y_{F,s}\, 4\pi R_s^2\, \rho_s\left(u_s - \frac{dR}{dt})_s\right)$$

$$-4\pi(\rho D)R_s^2 \frac{\partial Y_F}{\partial r})_s Y_{F,s} = \frac{Y_{F,MH}\left(\frac{\rho_{BM}}{\rho D}\frac{dR}{dt})_s - \frac{\dot{m}_{BM}Z}{R_s^2}\right) - \frac{\dot{m}_g Z}{R_s^2}\frac{\nu Y_{O_2,\infty}}{1-\exp\left(+\frac{\dot{m}_g Z}{R_s}\right)}}{\frac{\dot{m}_g Z}{R_s^2}\frac{1}{E_s - 1} + \frac{\rho_s}{\rho D}\frac{dR}{dt})_s} \tag{27}$$

The carbon dioxide mass fraction at the outer surface will be deduced in the same manner. We assume that no carbon dioxide has diffused into the bubbly mixture.

$$0 = Y_{CO_2,s}\left(\frac{\dot{m}_g Z}{R_s^2} - \frac{\rho_s}{\rho D}\frac{dR}{dt})_s\right) - \frac{dY_{CO_2}}{dr})_s$$

$$0 = Y_{CO_2,s}\left(\frac{\dot{m}_g Z}{R_s^2} - \frac{\rho_s}{\rho D}\frac{dR}{dt})_s\right) - \frac{\dot{m}_g Z}{R_s^2} \times (Y_{CO_2,s} - Y_{CO_2,\infty} - \nu\nu_4 Y_{O_2,\infty})\frac{E_s}{E_s - 1}$$

$$Y_{CO_2,s} = \frac{\frac{\dot{m}_g Z}{R_s^2}(Y_{CO_2,\infty} + \nu\nu_4 Y_{O_2,\infty})\frac{E_s}{E_s - 1}}{\frac{\dot{m}_g Z}{R_s^2}\frac{1}{E_s - 1} + \frac{\rho_s}{\rho D}\frac{dR}{dt})_s} \tag{28}$$

The water mass balance at the outer surface is phrased in a similar fashion. Yet, since the water mass fraction is evaluated through phase equilibrium, the water mass balance is used to evaluate the regression or progression rate of the outer surface.

$$\dot{m}_{H_2O,BM,s} = \dot{m}_{H_2O,g,s} - 4\pi(\rho D)R_s^2 \frac{\partial Y_{H_2O}}{\partial r})_s$$

$$Y_{H_2O,MH}\frac{\dot{m}_{BM}Z}{R_s^2} - Y_{H_2O,MH}\frac{\rho_{BM}}{\rho D}\frac{dR}{dt})_s = Y_{H_2O,s}\frac{\dot{m}_g Z}{R_s^2} - Y_{H_2O,s}\frac{\rho_s}{\rho D}\frac{dR}{dt})_s - \frac{\partial Y_{H_2O}}{\partial r})_s$$

$$\frac{dR}{dt})_s = \frac{Y_{H_2O,MH}\frac{\dot{m}_{BM}Z}{R_s^2} + Y_{H_2O,s}\frac{\dot{m}_g Z}{R_s^2}\frac{1}{E_s - 1} - \frac{\dot{m}_g Z}{R_s^2}\left(Y_{H_2O,\infty} + \nu\nu_3 Y_{O_2,\infty}\right)\frac{1}{1-\exp\left(+\frac{\dot{m}_g Z}{R_s}\right)}}{\left(Y_{H_2O,MH}\frac{\rho_{BM}}{\rho D} - Y_{H_2O,s}\frac{\rho_s}{\rho D}\right)} \tag{29}$$

The sum of the mass fractions equals unity; hence, the nitrogen mass fraction can be calculated.

Auxiliary mass relations: Using the global mass balance at the interface, we obtain auxiliary relations between the different mass fluxes

$$\dot{m}_{vap} = 4\pi R_s^2 \rho_{BM}\left(u_{BM,s} - \frac{dR}{dr})_s\right) = 4\pi R_s^2 \rho_s\left(u_{g,s} - \frac{dR}{dr})_s\right) \tag{30}$$

where $\dot{m}_{vap}$ is the bubbly mixture mass flow rate, relative to the droplet surface $\dot{m}_{BM,rel}$.

Since the vaporization mass flux is the bubbly mixture mass flux relative to the surface $\dot{m}_{vap} = \dot{m}_{BM,rel}$

$$\dot{m}_{vap} = \dot{m}_{BM} - 4\pi R_s^2 \rho_{BM}\frac{dR}{dr})_s = \dot{m}_g - 4\pi R_s^2 \rho_s \frac{dR}{dr})_s$$

$$\dot{m}_g = \dot{m}_{vap} + 4\pi R_s^2 \rho_s \frac{dR}{dr})_s$$

and

$$\dot{m}_g = \dot{m}_{BM} - 4\pi R_s^2 \frac{dR}{dr})_s(\rho_{BM} - \rho_s) \tag{31}$$

2.2.2. Energy balance

Heat that is conducted into the bubbly mixture from the gas phase, $\dot{q}_{g,s}$, both elevates its temperature, $\dot{q}_{BM,s}$, and evaporates the liquid $\dot{q}_{vap}$.

$$\dot{q}_{g,s} - \dot{q}_{L,s} = \dot{q}_{vap}$$

$$4\pi R_s^2\left(\lambda_g \frac{dT_g}{dr})_s - \lambda_{BM}\frac{\partial T_{BM}}{\partial r})_s\right) = Y_{H_2O,MH}\dot{m}_{vap}L_{vap} \tag{32}$$

In order to obtain the temperature gradient as a function of the mass flow rate and the surface properties, a linear combination of the first two S–Z functions is constructed.

$$\beta_T = \beta_2 - \beta_1 = \frac{C_{p,g}}{Q_F}(T_g - T_\infty) + \nu(Y_{O_2} - Y_{O_2,\infty}) \tag{33}$$

The temperature gradient at the surface is obtained by deriving the new S–Z function and applying thin flame assumptions.

$$\frac{d\beta_T}{dr})_s = \frac{dT_g}{dr})_s = \frac{\dot{m}_g Z}{R_s^2}\left[(T_s - T_\infty) - \frac{\nu Q_F}{C_{p,g}}Y_{O_2,\infty}\right]\frac{1}{1 - \exp\left(+\frac{\dot{m}_g Z}{R_s}\right)} \tag{34}$$

The thermal conductivity of the bubbly mixture is equal to that of the water, $\lambda_{BM} = \lambda_L$.

$$\frac{\partial T_{BM}}{\partial r})_s = \frac{\lambda_g}{\lambda_{BM}}\frac{dT_g}{dr})_s - \frac{\dot{m}_{vap}Y_{H_2O,MH}L_{vap}}{4\pi R_s^2 \lambda_{BM}}$$

$$\frac{\partial T_{BM}}{\partial r})_s = \frac{\lambda_g}{\lambda_{BM}}\frac{\dot{m}_g Z}{R_s^2}\left[(T_s - T_\infty) - \frac{\nu Q_F}{C_{p,g}}Y_{O_2,\infty}\right] \times \frac{1}{1 - \exp\left(+\frac{\dot{m}_g Z}{R_s}\right)} - \frac{\dot{m}_{vap}Y_{H_2O,MH}L_{vap}}{4\pi R_s^2 \lambda_{BM}} \tag{35}$$

2.3. Bubbly mixture

2.3.1. Transient temperature distribution

Heat from the gas phase is conducted into the liquid shell, heating it as its boundaries regress. Heat transfer within the liquid shell is slow compared to heat transfer within the gas; thus, the bubbly-mixture heat conduction should be treated as transient with moving boundaries. Part of the heat melts the solid core of the hydrate, releasing small methane bubbles that follow the water mass flux. Moreover, the density of a solid hydrate ($\rho_{hydrate} = 0.912$ g/cc) [3] is similar to that of pure ice ($\rho_{ice} = 0.9167$ g/cc) [19]. Yet, the difference in densities between the solid hydrate and the melted water 0.9998 g/cc) will induce advection as well, in the opposite (i.e., negative radial) direction. We will neglect the effect based upon the very small density difference.

The resulting bubbly mixture energy equation with advection of both the water and the methane enthalpy (with no chemical reaction within bubbly mixture) for an average value of thermal diffusivity becomes

$$\rho_{BM} r^2 C_{p,BM}\frac{\partial T_{BM}}{\partial t} + \left(\rho u r^2 C_p\right)_{BM}\frac{\partial T_{BM}}{\partial r} = \lambda_{BM}\frac{\partial}{\partial r}\left(r^2\frac{\partial T_{BM}}{\partial r}\right) \tag{36}$$

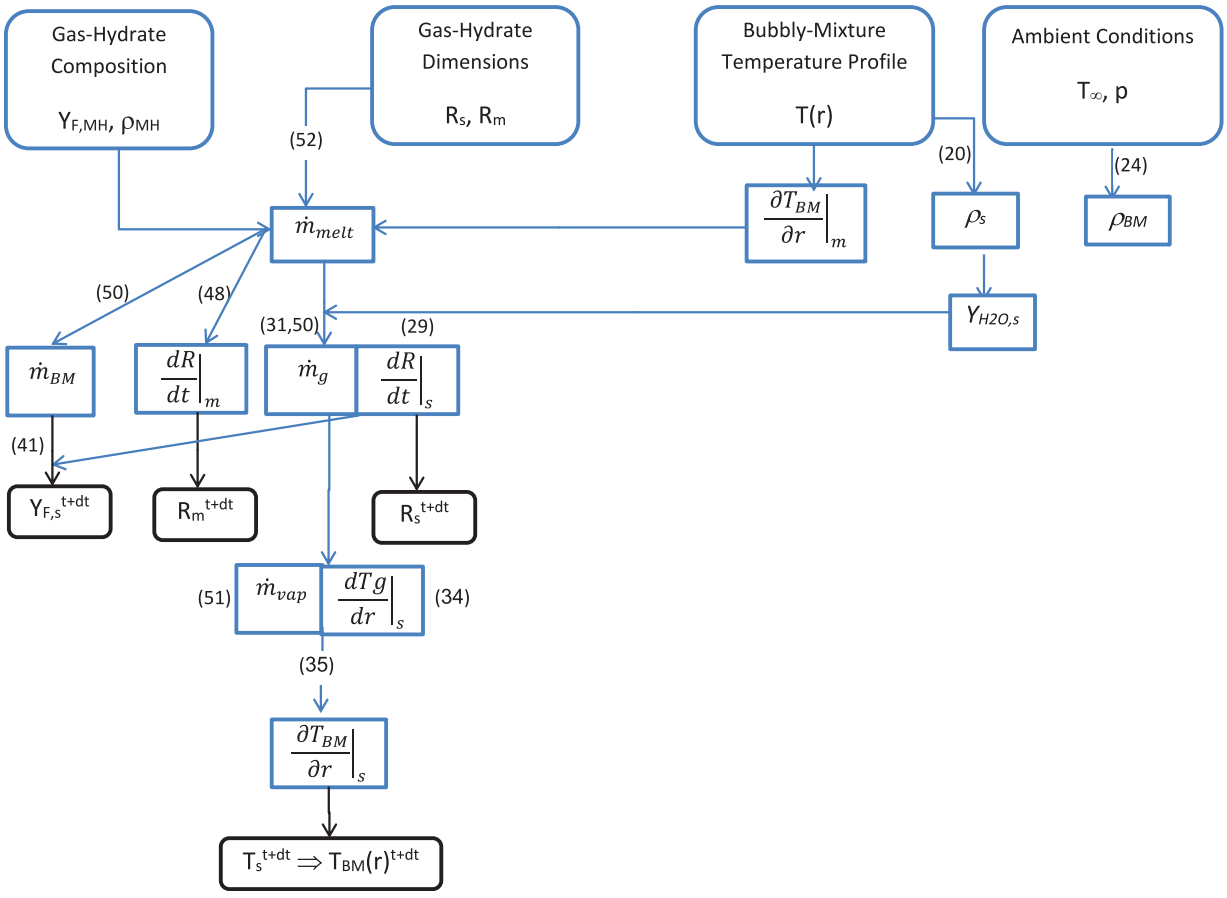

Fig. 3. Solution procedure – small methane bubbles.

dividing by $(\rho r^2 C_p)_{BM}$

$$\frac{\partial T_{BM}}{\partial t} = \alpha_{BM}\frac{\partial^2 T_{BM}}{\partial r^2} + \left(\frac{2\alpha_{BM}}{r} - u_{BM}\right)\frac{\partial T_{BM}}{\partial r} \tag{37}$$

The methane bonding with the water is broken upon melting. Negligible methane dissolves in the liquid water due to low Henry constants.

Thermophysical properties of melted methane-hydrates are found for a limited range of temperatures, i.e. −20–17 °C [21–23]. Moreover, since the thermal conductivity of methane-hydrate is approximately equal to that of water, and since the methane is dispersed throughout the water, and is roughly 15% of the mixture mass at the highest natural loading, the thermal conductivity value of the mixture is dominated by the liquid water value. Since the methane does not dissolve in the water, then the thermal diffusivity of the mixture is evaluated as the water thermal conductivity divided by the product of the density and the mixture heat capacity.

$$\alpha_{BM} = \frac{\lambda_{H_2O}}{\rho_{BM} C_{p,BM}}, \qquad C_{p,BM} = Y_{H_2O,BM,s}\, C_{p,H_2O,L} + Y_{F,BM,s} C_{p,F,g} \tag{38}$$

The problem is transformed to a boundary problem with the outer boundary fixed by defining non-dimensional variables $\eta \equiv r/R_s(t)$.

$$\frac{R_s^2}{\alpha_{BM}}\frac{\partial T_{BM}}{\partial \tau} = \frac{\partial^2 T_{BM}}{\partial r^2} + \frac{2}{\eta}\left(1 - \frac{R_s u_{BM}}{2\alpha_{BM}}\eta - \frac{K_1}{4\alpha_{BM}}\eta^2\right)\frac{\partial T_{BM}}{\partial \eta} \tag{39}$$

where $C_{advc} = R_s u_{BM}/(2\alpha_{BM})$

The following boundary conditions apply:

$$T_{BM}(\eta_m) = T_{melt}, \quad T_{BM}(1) = T_s(t) \tag{40}$$

Once the solid core is fully melted, the boundary condition appropriate for the center of a spherical droplet is used.

$$\frac{\partial T_{BM}}{\partial \eta})_{\eta=0} = 0 \tag{41}$$

K_1 is proportioned to the instantaneous rate of change of particle surface area.

$$K_1(t) \equiv -2R_s(t)\frac{dR_s(t)}{dt}$$

$$R_s^2(t_n) = R_s^2(t_{n-1}) + \int \frac{dR_s^2}{dt}dt = R_s^2(t_{n-1}) - \int_{t_{n-1}}^{t_n} K_1 dt \tag{42}$$

2.3.2. Radial velocity of the condensed phase

The density of the bubbly mixture is lower than the ice density. Therefore, melting causes an outward motion of the bubbly mixture with radial velocity u_{BM}. At the melting surface that velocity is $u_{BM,m}$. Consequently,

$$\dot{m}_{melt} = 4\pi R_m^2 \rho_{BM}\left(u_{BM,m} - \frac{dR_m}{dt}\right) \tag{43}$$

We define the radii ratio K_2 as

$$K_2(t) \equiv \frac{R_s(t)}{R_{ls}(t)} \tag{44}$$

Thus,

$$\frac{dK_2}{dt} = \frac{1}{R_m}\frac{dR_s}{dt} - \frac{R_s}{R_m^2}\frac{dR_m}{dt} \tag{45}$$

where the change rates of the outer and inner surfaces are taken from Eqs. (29) and (48)

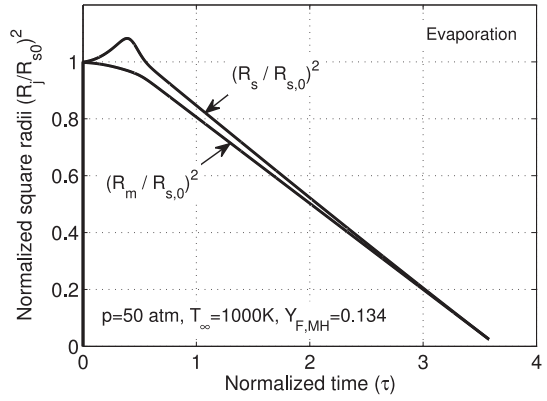

(a) History of hydrate radii

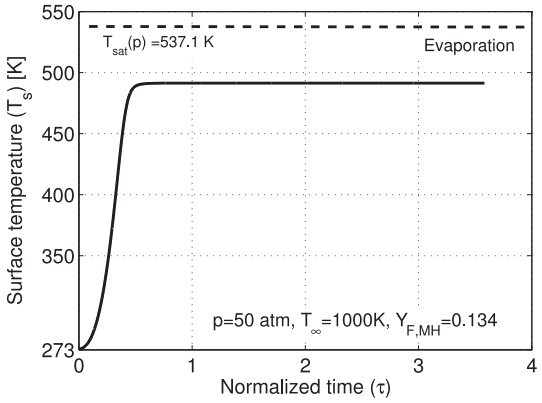

(b) Surface temperature

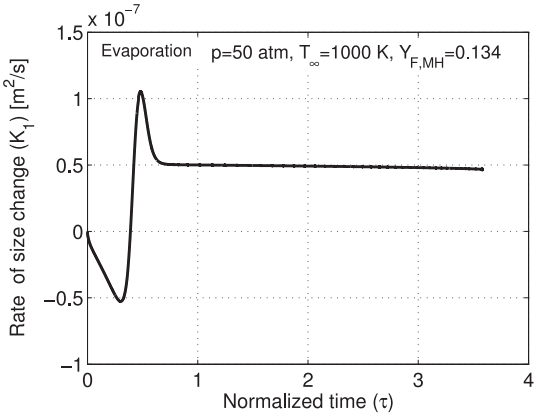

(c) Rate of size change

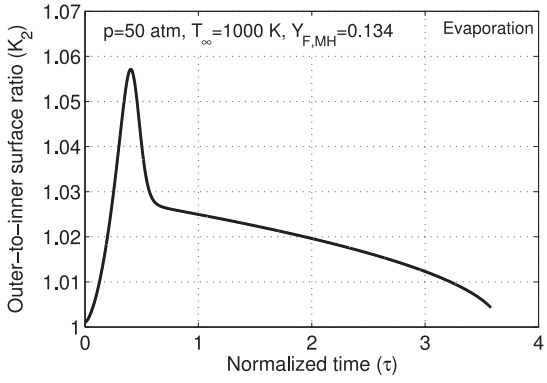

(d) Outer-to inner surface ratio

Fig. 4. Evaporation – surface values; p =50 atm, T_∞=1000 K, $Y_{F,MH}$ = 0.134.

Thus,

$$R_m^2 \frac{dR_m}{dt} = \left(\frac{R_s}{K_2}\right)^2 \left(\frac{1}{K_2}\frac{dR_s}{dt} - \frac{R_s}{K_2^2}\frac{dK_2}{dt}\right) = -\frac{K_1 R_s}{2K_2^3} - \frac{R_s^3}{K_2^4}\frac{dK_2}{dt} \tag{46}$$

u_{BM} can be shown to vary inversely with the square of the radius through the bubbly mixture.

$$u_{BM} = \frac{\dot{m}_{melt}}{4\pi\rho_{BM} r^2} + \left(\frac{R_m}{r}\right)^2 \frac{dR_m}{dt}$$

$$u_{BM} = \frac{1}{\eta^2}\left(\frac{\dot{m}_{melt}}{4\pi\rho_{BM} R_s^2} - \frac{K_1}{2R_s K_2^3} - \frac{R_s}{K_2^4}\frac{dK_2}{dt}\right) \tag{47}$$

2.4. Solid phase

2.4.1. Mass balance

The melting mass flux in the laboratory frame, $\dot{m}_{melt}$, is

$$\dot{m}_{melt} = 4\pi R_m^2 \rho_{MH}\left(-\frac{dR}{dt}\right)_m \tag{48}$$

where R_m is the position of the melting interface.

The difference between the densities of the hydrate and the bubbly mixture result in the advection velocity u_{BM} through the bubbly mixture. Thus,

$$\dot{m}_{melt} = 4\pi R_m^2 \rho_{BM}\left(u_{BM,m} - \frac{dR}{dr})_m\right) \tag{49}$$

or

$$\dot{m}_{BM} = \dot{m}_{melt}\left(1 - \frac{\rho_{BM}}{\rho_{MH}}\right) \tag{50}$$

The change in volume of the bubbly mixture is simply related to the difference between melting rate and vaporization rate.

$$\dot{m}_{vap} - \dot{m}_{melt} = 4\pi\rho_{BM}\left(R_m^2 \frac{dR}{dr})_m - R_s^2 \frac{dR}{dr})_s\right) \tag{51}$$

2.4.2. Energy balance

Heat that is conducted into the solid core melts the frozen core which remains at constant temperature.

$$\dot{q}_m = \dot{q}_{melt}$$

$$4\pi R_m^2 \frac{\lambda_{BM}}{R_s}\frac{\partial T_{BM}}{\partial \eta})_m = Y_{H_2O_{MH}} \dot{m}_{melt} L_{melt} \tag{52}$$

The melting mass flow rate could be deduced by the above expression, once the temperture distribution within the bubbly mixture is resolved (see Section 2.3) and the temperature gradient at the inner surface ($\frac{\partial T_{BM}}{\partial \eta})_m$) is calculated.

3. Solution procedure

When a cold hydrate is introduced into a hot environment, it undergoes melting and evaporation processes. Namely, the right side of the species and energy equations (Eqs. (2) and (6)) are zeroed. If the ambient temperature were sufficiently high, the methane would

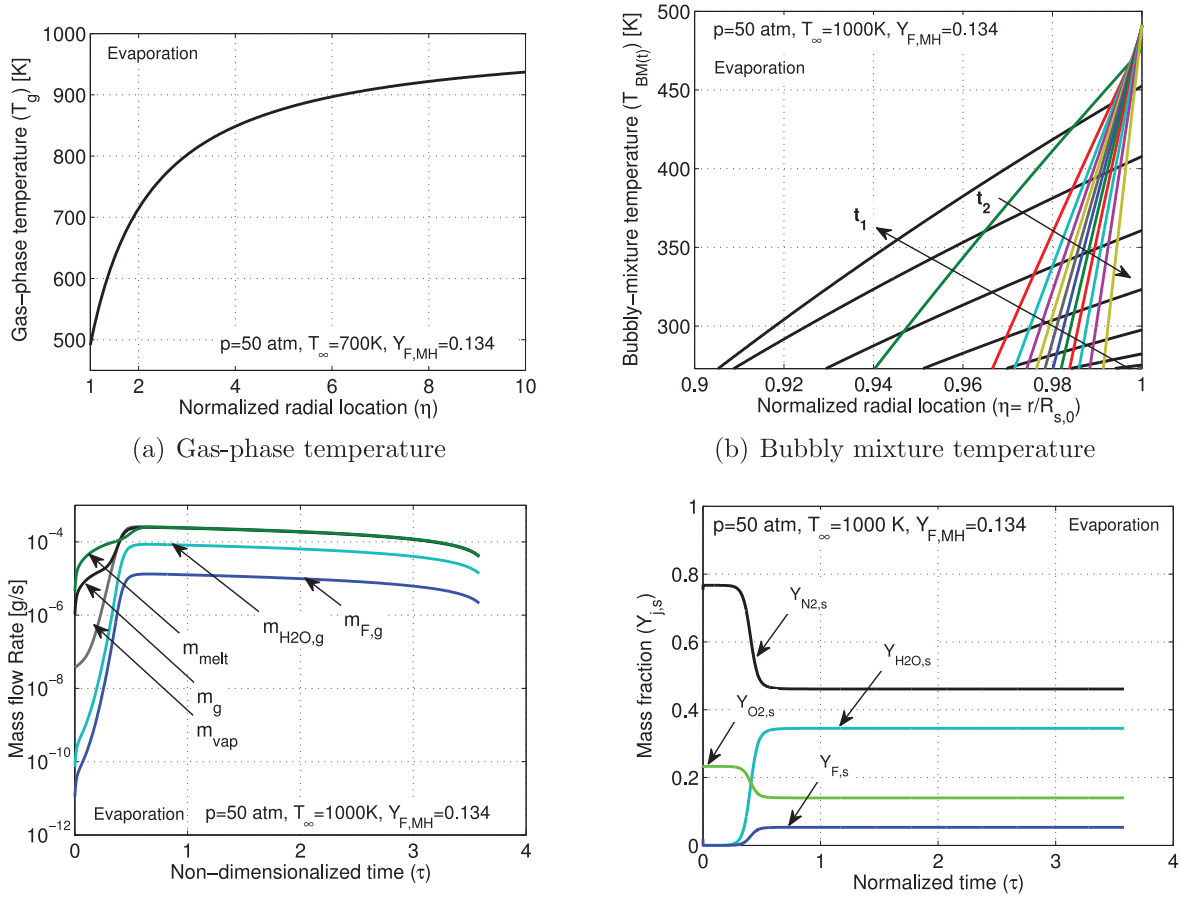

(a) Gas-phase temperature

(b) Bubbly mixture temperature

(c) Mass flow rates

(d) Surface mass fractions

Fig. 5. Evaporation; p =50 atm, T_∞=1000 K, $Y_{F,MH}$ = 0.134.

ignite after an induction period. Since the methane-hydrate is to be used as a fuel, it can be ignited by external means and burn even at low ambient temperatures. Fig. 3 presents the synopsis of the solution procedure for the combustion process.

For given hydrate composition ($Y_{F,MH}, Y_{H_2O,MH}$) and thermodynamic conditions of the surroundings (air at given temperature T_∞ and pressure p), a spherical bubbly mixture is assumed to exist. The melting mass flow rate is calculated ($\dot{m}_{melt}$ Eq. (52)) from which the regression rate of the inner interface ($(\frac{dR}{dt})_m$ Eq. (48)) and the bubbly-mixture mass flow rate ($\dot{m}_{BM}$ Eq. (49)) are deduced. The total vaporization mass flux ($\dot{m}_g$) and the rate change of the outer surface ($(\frac{dR}{dt})_s$) are then computed simultaneously by Eqs. (31) and (29). Knowing the total evaporating mass flux means that the gas-phase solutions can be calculated (Section 2.1). Now, the gas-phase temperature gradient at the outer interface is known ($(\frac{dT_g}{dr})_s$ Eq. (34)) and is substituted into the energy balance to calculate the temperature gradient at the liquid side (Eq. (32)). Together with the freezing temperature at the liquid–solid interface, we now have two boundary conditions and the heat-diffusion equation (Eq. (39)) within the bubbly mixture is solved numerically by the Crank–Nicholson method. The radial domain of the bubbly-mixture was divided exponentially to 500 unequal spaces, where the smallest space is adjacent to the inner surface, where the gradients are the steepest. The time step varied between 0.01 ms and 0.1 ms, depending on the analyzed process (evaporation or combustion) for a typical particle of 100 μm. A new surface temperature and hydrate radii are then computed for the next time step.

3.1. Evaporation only

In the event of pure evaporation, where $Q = 0$, the temperature gradient at the surface simplifies to the classic evaporation expression.

$$\frac{dT_g}{dr})_{s,evap} = \frac{\dot{m}_s Z}{R_s^2}(T_\infty - T_s)\frac{E_s}{1-E_s} \tag{53}$$

During evaporation, knowledge of the surface conditions allows the evaluation of the radial profiles of the mass fractions using the homogeneous, linear, 2nd order species equation.

$$\begin{aligned} Y_{F,evap}(r) &= Y_{F,\infty} + (Y_{F,s} - Y_{F,\infty})\frac{\exp(-\frac{\dot{m}_g Z}{r}) - 1}{E_s - 1} \\ Y_{H_2O,evap}(r) &= Y_{H_2O,\infty} + (Y_{H_2O,s} - Y_{H_2O,\infty})\frac{\exp(-\frac{\dot{m}_g Z}{r}) - 1}{E_s - 1} \\ T_{g,evap}(r) &= T_\infty + (T_s - T_\infty)\frac{\exp(-\frac{\dot{m}_g Z}{r}) - 1}{E_s - 1} \end{aligned} \tag{54}$$

For evaporation, the following expressions could be obtained from the thin flame expression by setting $\nu = 0$, $Q_F = 0$:

$$\frac{dY_F}{dr})_{s,evap} = Y_{F,s}\frac{\dot{m}_g Z}{R_s^2}\frac{E_s}{E_s - 1} \tag{55}$$

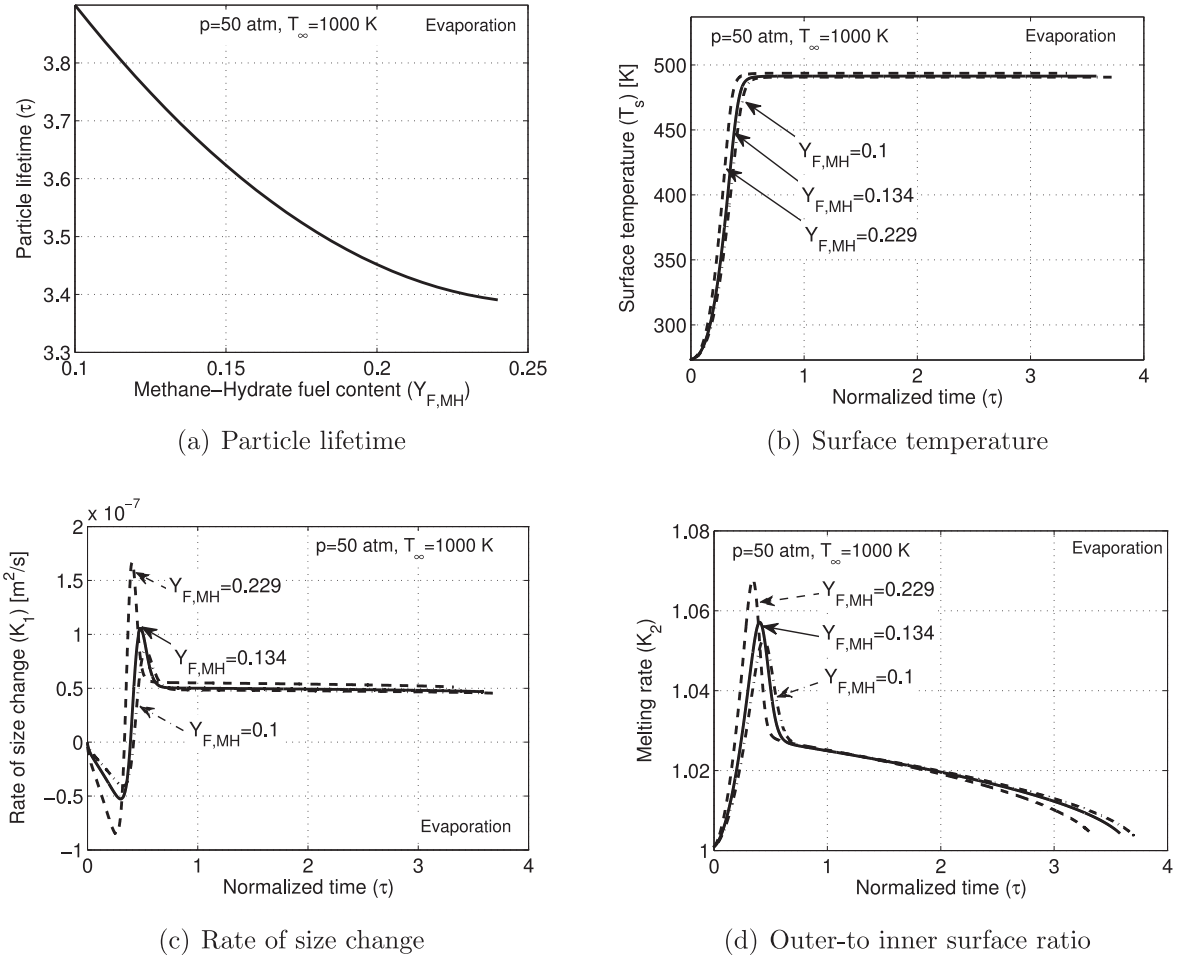

(a) Particle lifetime

(b) Surface temperature

(c) Rate of size change

(d) Outer-to inner surface ratio

Fig. 6. Evaporation at different fuel contents; $p = 50$ atm, T_∞=1000 K, $Y_{F,MH}$= 0.1, 0.134, 0.229.

$$Y_{F,s,evap} = Y_{F,MH}\frac{\frac{\rho_{BM}}{\rho D}\frac{dR}{dt})_s - \frac{\dot{m}_{BM}Z}{R_s^2}}{\frac{\dot{m}_g Z}{R_s^2}\frac{1}{E_s - 1} + \frac{\rho_s}{\rho D}\frac{dR}{dt})_s} \tag{56}$$

$$Y_{O_2,s,evap} = \frac{1 - (Y_{F,s} + Y_{H_2O,s})}{1 + \frac{m_{N_2}}{m_{O_2}}} \tag{57}$$

3.2. Combustion

Once the surface temperature is sufficiently high to sustain combustion, both the species and energy equations become non-homogeneous, non-linear, 2nd order equations.

Combustion at infinite chemical reaction rates is considered and referred to as “thin flame”. That is, the reaction zone collapses to a mathematical interface where the reactants meet in stoichiometric proportion [24]. The oxygen concentration at and near the bubbly mixture–gas interface becomes zero. The radial position of the flame (R_f) is determined by the place at which the values of both the fuel and oxygen mass fractions are zero.

$$\alpha_1(R_f) = \nu Y_{O_2,\infty} = (Y_{F,s} + \nu Y_{O_2,\infty})\frac{\exp(-\frac{\dot{m}_g Z}{R_f}) - 1}{E_s - 1}$$

$$R_f = -(\dot{m}_g Z)/\ln\left(\frac{Y_{F,s} + \nu Y_{O_2,\infty}E_s}{Y_{F,s} + \nu Y_{O_2,\infty}}\right) \tag{58}$$

In this case, the species and energy equations remain linear; however, the radial profiles of the temperature and gas species are determined by the Shvab–Zel’dovich functions, under different constraints at the inner and outer zones. In the inner zone between the particle and the flame, there is no oxygen, while in the outer zone, spanning from the flame to infinity, there is no fuel.

$$R_s \le r \le R_f, \quad Y_{O_2} = 0$$

$$Y_{H_2O} = \beta_2, \quad Y_F = \frac{\beta_1 - Y_{H_2O}}{m_4} \tag{59}$$

$$R_f \le r \le \infty, \quad Y_F = 0$$

$$Y_{H_2O} = \beta_1, \quad Y_{O_2} = \frac{\beta_2 - Y_{H_2O}}{m_4\nu} \tag{60}$$

$$Y_{CO_2} = \frac{m_3}{m_4}(Y_{H_2O} - \beta_4) \tag{61}$$

$$T = \frac{QY_{H_2O} - \beta_3}{m_4 C_{p,g}} \tag{62}$$

4. Results and discussion

When all cavities of the hydrate are filled, the methane-hydrate mole fractions are 0.852 for water and 0.148 for methane [7]. Accordingly, mass fraction of the fuel within the hydrate is 0.134 ($Y_{F,MH}$ = 0.134), and an average methane-hydrate composition of one mole of methane for every 5.75 moles of water is attained.

Under the quasi-steady gas-phase assumption with no radiation or buoyancy for the gas-phase, the only characteristic time for the analysis is the liquid-phase diffusion time $R_{s,0}^2/\alpha_{BM,0}$. The results in this section address particles of a typical radius of 100 μm or less. For

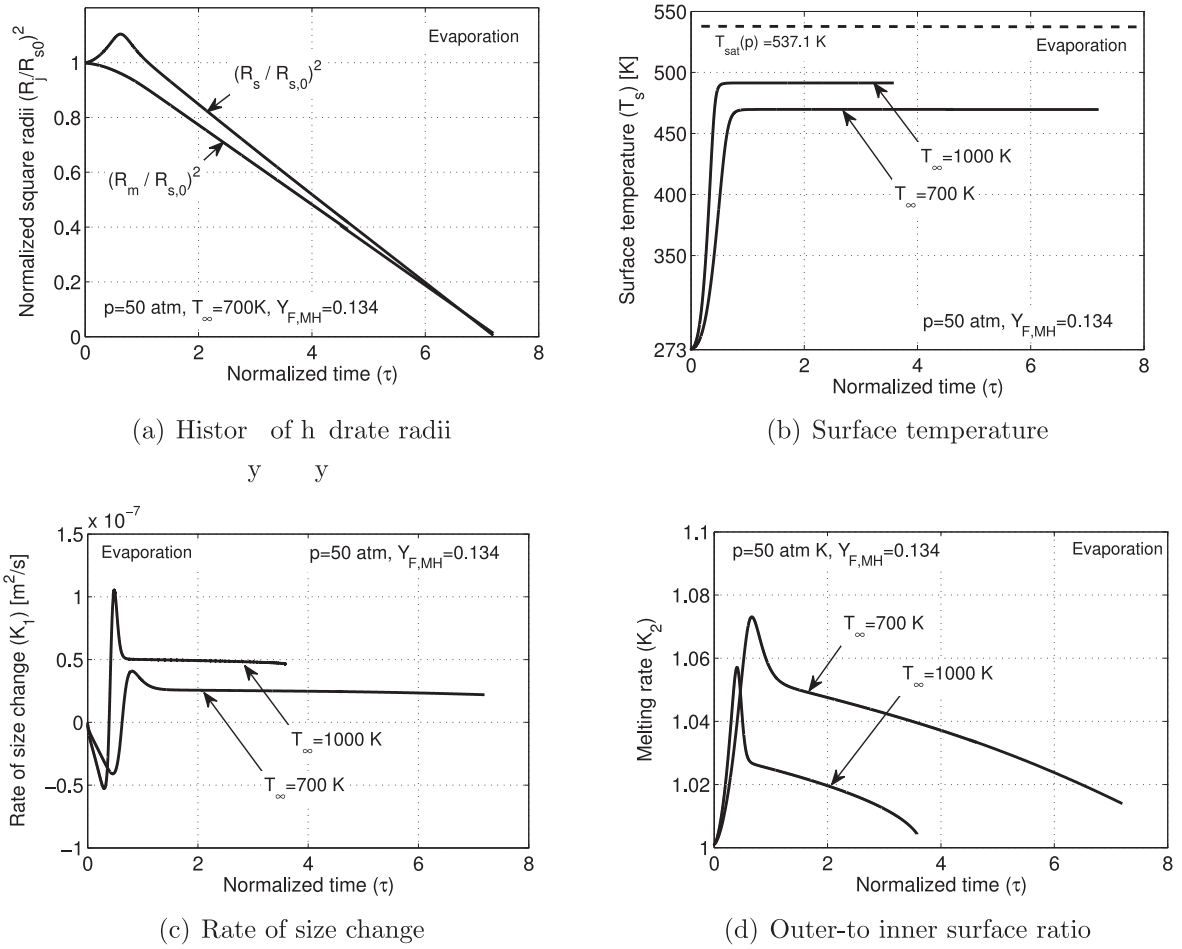

(a) History of hydrate radii

(b) Surface temperature

(c) Rate of size change

(d) Outer-to inner surface ratio

Fig. 7. Evaporation at different ambient temperatures; p =50 atm, T_∞=700, 1000 K, $Y_{F,MH}$ = 0.134.

convenience in scaling, that time constant is used to normalize the dimensional time ,$\tau \equiv t/\left(R_{s,0}^2/\alpha_{BM,0}\right)$, while $R_{s,0}$ is used to normalize radial position. For these conditions, the non-dimensional solution does not depend on the initial radius value. Thus, scaling is a simple exercise.

4.1. Evaporation

High ambient temperature drives the melting and evaporation processes. Thus, as time develops, the inner interface of the particle recedes (R_m decreases, $K_2 > 0$, Fig. 4a and d). The hydrogen bonds break due to the melting process and methane is released. The methane and water that broke free from the matrix create a bubbly mixture that first expands, leading to the progression of the outer surface ($0 < \tau < 0.34$, R_s increases, $K_1 < 0$, Fig. 4a and c). The species composition of the bubbly mixture is assumed to be the same as its composition within the hydrate; however, the densities are determined by the averaged mixture temperature that increases with time (in accordance to the surface temperature (Fig. 4b)), thus decreasing densities (Eq. (24)). As a result, the particle expands ($\tau < 0.39$, $K_1 > 0$).

The gas-phase temperature monotonically increases with radius from its surface value to the ambient value (Fig. 5a)).

The swelling and shrinkage effect can be seen also by observing the bubbly-mixture temperature (Fig. 5b). As long as the bubbly-mixture contains water and methane, the surface temperature is lower than the boiling and saturation temperatures for pure water ($T_{sat,H_2O}(p = 50\,\text{atm}) = 537.09$ K). Namely, the bubbly-mixture temperature continuously rises until it reaches its appropriate "wet-bulb temperature" (496 K, Fig. 4b). During this time (t_1), the outer-to-inner ratio increases as well. Then, the particle starts to shrink (t_2).

The amount of heat flux changes with the temperature differences at the surface and with the bubbly-mixture thickness. During the initial period, a greater heat flux is used to elevate the liquid temperature and to melt the ice. Thus, the melting rate ($\dot{m}_{melt}$) at the beginning of the process is higher than the evaporation rate ($\dot{m}_g$) (Fig. 5c) due to higher temperature gradients at the icy interface. As time passes, the thickness of the bubbly mixture increases, more heat is conducted into it, and the surface temperature rises. The outer-to-inner radii ratio (K_2) continues to increase until the evaporation rate exceeds that of the melting. Moreover, during the swelling period, the vaporization mass flux ($\dot{m}_{vap}$) is higher than the gas-phase mass flux ($\dot{m}_g$) since the rate change of the outer radius is positive (Eq. (31)). For a nominal hydrate composition ($Y_{F,MH} = 0.134$) that happens at $\tau = 0.4$ (Fig. 5c).

As the surface temperature increases, the water mass fraction, that mainly depends on the partial water vapor pressure at the surface, increases as well ($Y_{H_2O,s}$ (Fig. 5d)). Along with a small increase in the fuel mass fraction, it leads to the decrease of the air mass fraction at the surface. After a while ($\tau \approx 0.75$), the processes relaxes to nearly constant values, as for a d^2-law case.

4.1.1. Hydrate fuel content effect

When all hydrate cavities are filled, the ratio of water-to-methane molecules is 5.75. However, when the hydrate cavities are not filled with methane, as often happens in naturally occurring hydrates and in laboratory experiments due to partial dissociation of methane, the methane mass fraction at the gas side will decrease. Less methane

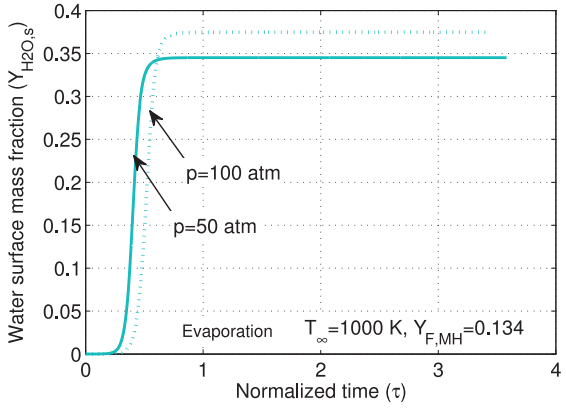

(a) History of hydrate radii

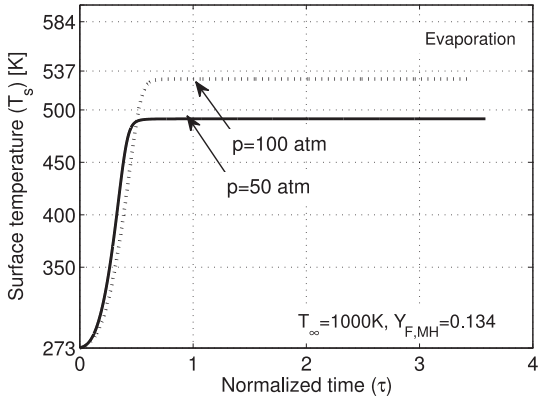

(b) Surface temperature

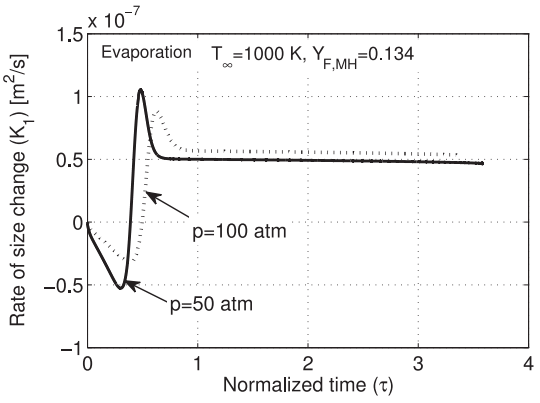

(c) Rate of size change

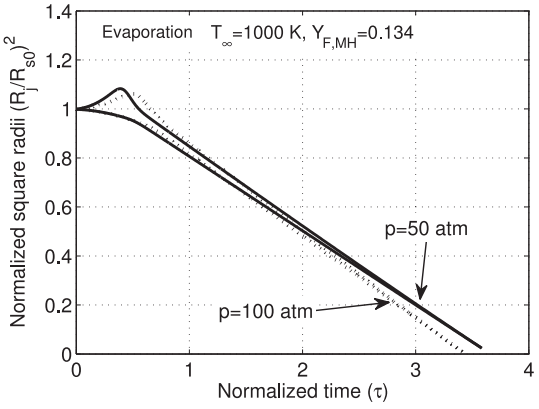

(d) Outer-to inner surface ratio

Fig. 8. Evaporation at different ambient temperatures; p =50, 100 atm, T_∞=1000 K, $Y_{F,MH}$ = 0.134.

means higher water content. As a result, more heat is required to heat the liquid during the initial period, prolonging the particle lifetime. For example, reduction of 25% of the fuel content from $Y_{F,MH} = 0.134$ to $Y_{F,MH} = 0.1$ results in extension of about 10% of the particle lifetime (Fig. 6a). For the same reason, the increase in the surface temperature is slightly slower (Fig. 6b). The slow increase in the surface temperature results in a more negative value of the evaporation rate, represented by K_1 (Fig. 6c), and yet to a small decrease in the outer-to-inner surface ratio (K_2, Fig. 6d). The effect becomes even less noticeable as the fuel content increases. The fuel content effect will be more distinct when combustion prevails (Section 4.2.1)

4.1.2. Ambient temperature effect

By lowering the ambient temperature, we reduce the driving force of the process; thereby lowering all transport rates, and lengthening the particle lifetime (Fig. 7a and b). For example, at ambient temperature of 700 K, the particle lifetime is $\tau \approx 7.6$, while for $T_\infty = 1000$ K it is completely evaporated at approximately half of that time. The evaporation rate is slower for lower ambient temperature (Fig. 7c). Though both the evaporation and melting rates are slower for lower ambient temperatures, their relative ratio is not lower, and the outer-to-inner surface ratio (K_2) is higher for $T_\infty = 700$ K than for $T_\infty = 1000$ K. Moreover, it reaches its maximal value later (Fig. 7d).

4.1.3. Ambient pressure effect

Higher ambient pressure induces higher wet-bulb temperature. Figure 8 presents comparison between 50 atm (bold curves) and 100 atm (dotted curves). For example, ambient pressure of 100 atm corresponds to a wet-bulb temperature of 536 K, as compared to 496 K for an ambient pressure of 50 atm. The higher wet-bulb temperature causes the water mass fraction at a given temperature to be initially lower for higher ambient pressures (Fig. 8a). As a result, its difference across the outer surface decreases as well, leading to lower K_1 value, and a more moderate temperature increase of the surface temperature. This implies lower temperature gradients within the bubbly mixture; thereby an initial lower melting rate. However, due to the higher wet-bulb temperature, the surface temperature reaches higher values at $\tau \approx 0.5$ (Fig. 8b), trailing higher evaporation and melting rates from that moment on (Fig. 8c), and leads to a slightly shorter particle lifetime (Fig. 8d).

4.2. Infinite chemical reaction rate

There is no definite auto-ignition temperature for methane-hydrate. Nonetheless, since the auto-ignition temperature of methane-air mixtures at atmospheric pressure varies from 537 °C to 600 °C [25], it is expected that the methane-hydrate would auto-ignite at some higher temperatures.

Now, combustion at infinite chemical reaction rates is considered. In this case, the mass fraction of the oxygen at the surface obtains the value of zero $Y_{O_2,s} = 0$, and combustion is possible when the water mass fraction reaches a threshold value that would allow $R_f/R_s > 1$ (Fig. 9a). For the nominal conditions ($Y_{F,MH} = 0.134$), this would happen at $Y_{H_2O,s} > 0.4$ that corresponds to a surface temperature of $T_s \approx$

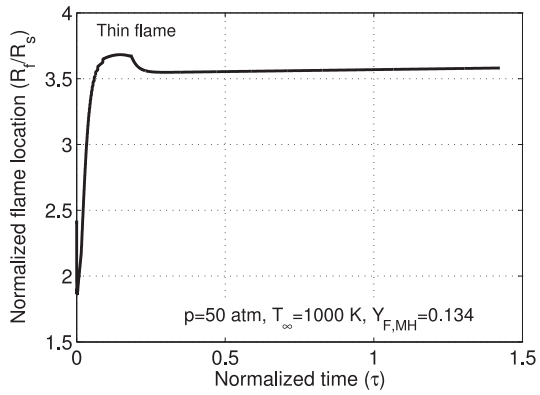

(a) Flame location

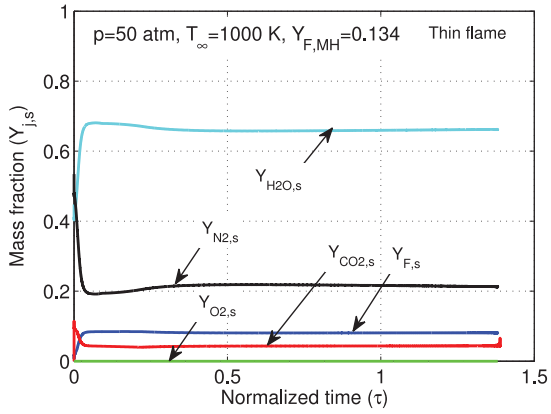

(b) Surface mass fractions

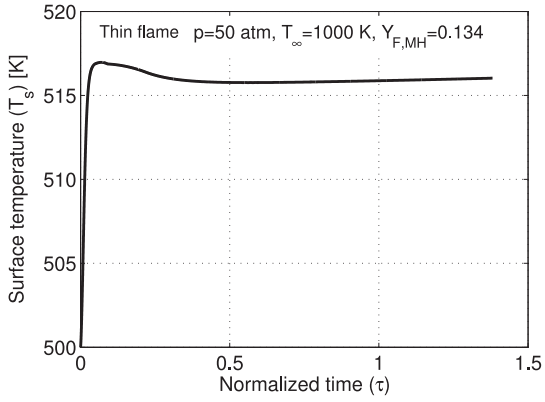

(c) Surface temperature

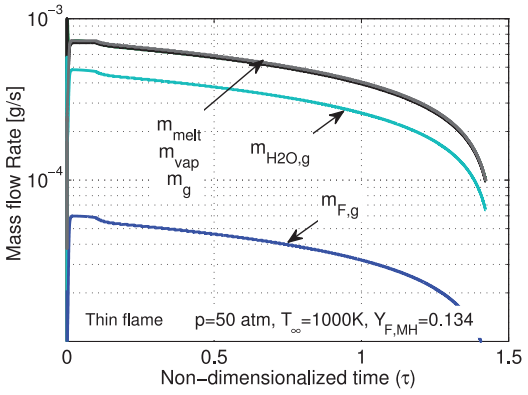

(d) Mass flow rates

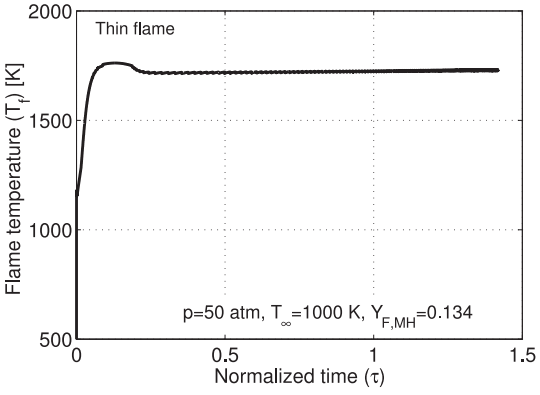

(e) Flame location

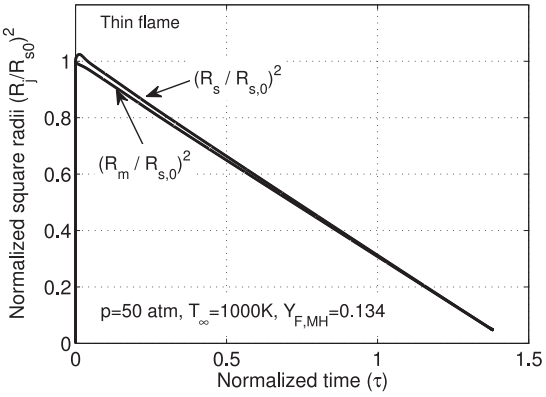

(f) History of hydrate radii

Fig. 9. Thin flame – temporal evolution; p= 50 atm, T_∞=1000 K, $Y_{F,MH}$ = 0.134.

500 K at 50 atm, as shown in Fig. 9b and c. These conditions are met by $\tau \simeq 0.5$ (Fig. 8a). At that time, the particle outer diameter slightly exceeds its initial value and its inner diameter is only slightly reduced (Fig. 8d). Once the particle reached the surface conditions that allow thin flame combustion, it is fully consumed by $\tau \simeq 1.5$ (Fig. 9). The flame location increases as long as both the surface temperature and the mass flux through the gaseous phase ($\dot{m}_g$, Fig. 9d) increase. It can be seen that the surface temperature escalates very rapidly during the short "swelling" period (Fig. 9f), and then relaxes to the appropriate wet-bulb temperature. On the other hand, the mass fluxes, decrease, creating a small peak in the flame temperature (Fig. 9e). The flame is pushed away from the surface as the flame temperature increases (Fig. 9a). In general, the transport processes for combustion are faster than for pure evaporation; thereby the particle lifetime is considerably shorter.

The bubbly mixture temperature distribution during the infinite chemical reaction rate is presented in Fig. 10. The surface temperature reaches the wet-bulb value (~517 K) by the end of the very brief swelling period (t_1, black curves); it remains there for the remainder of the lifetime (t_2).

Figure 11 a presents a typical radial profile of the mass fractions in the gas phase. The methane both advects and diffuses from the surface, while the oxygen diffuses from the environment towards the surface. The mass fractions of both the fuel (Y_F) and of the oxidizer

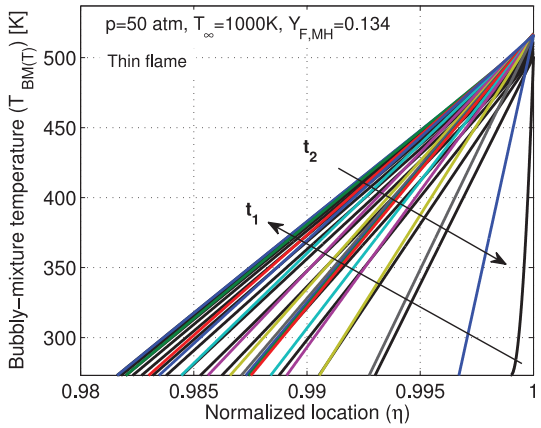

Fig. 10. Thin flame – temporal evolution; $p = 50$ atm, T_∞=1000 K, $Y_{F,MH} = 0.134$.

(Y_{O_2}) become zero at the flame location. The nitrogen, per contra, is not diminished by reaction and monotonically rises with radial position until it reaches its value at the surroundings. At infinity, for the considered case, there is no fuel, thus ($Y_{F,\infty} = Y_{CO_2,\infty} = Y_{H_2O,\infty} = 0$), but there is oxygen ($Y_{O_2,\infty} = 0.233$). By definition (Eq. (12)), the S–Z functions are zeroed at infinity, thus $\beta_{i,\infty} = 0$ (Fig. 11b). The location at which the fuel and oxygen meet, ($\eta \approx 3.5$) i.e. flame location, corresponds to the point at which the gas-phase temperature assumes its maximal value (Fig. 11c). During the combustion, conditions at the surface are fairly constant; thereby, the flame temperature and location are practically constant.

4.2.1. Hydrate fuel content effect

As stated, the ratio of 5.75 moles of water to every mole of methane is the theoretical maximum of methane-hydrate. Thus, it is likely that both lab-made methane hydrates and naturally occurring methane-hydrates with less methane content will be found. That will lead to a decrease in the fuel mass flow rate and evaporation rate. In addition, the effect of methane content expresses itself by the thermal diffusivity of the mixture through its heat capacity. However, this effect is small, as compared to the direct effect on the mass flow rate. The ratio of the mixture heat capacities values for $Y_{F,MH} = 0.1, 0.134$, is about 0.98; Thus, the heat diffusivity values are increased by about 2%. Less methane, or alternatively, more water, requires more heating per unit energy of combustion, as is well seen in the flame temperature and location. For example, for a methane-hydrate that contains 10% of methane by mass, namely $Y_{F,MH} = 0.1$ due to higher water quantity, the flame temperature is lower, i.e., $\sim$ 1500 K, as compared to 1700 K for the nominal hydrate, (see Fig. 12a) and the flame is located nearer to the surface: 2.7 vs 3.5 (Fig. 12b).

Higher methane-to-water ratio is similar to combustion with drainage. Namely, part of the melted water is drained from the bubbly mixture; thus, less heat is required to heat the bubbly mixture, although, the heat for melting remains the same with drainage. We can consider that drainage will cause similar trends to those shown in Fig. 12. For ambient temperature of 1000 K, the flame temperature will be as high as 2050 K for $Y_{F,MH} = 0.229$. For room ambient temperature (T_∞=300 K), it will be impossible for combustion to occur without some drainage. Since methane-air flames extinguish at temperatures around 1400 K, then combustion at room temperature will be possible for high methane-to-water ratios.

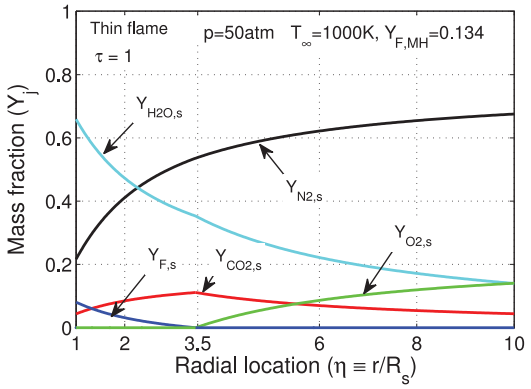

(a) Radial profile of the mass fractions

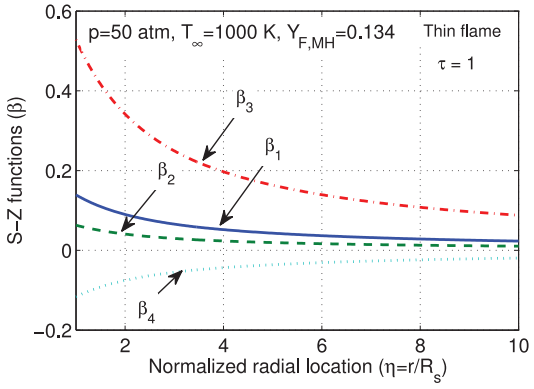

(b) Shvab-Zel'dovich functions

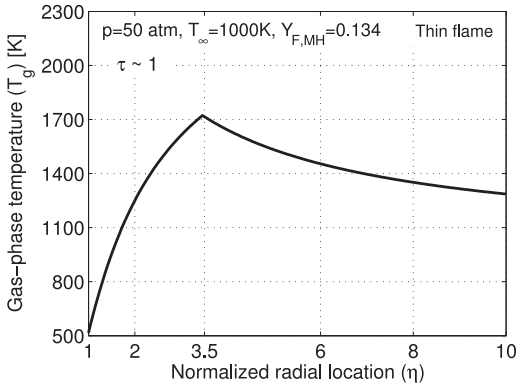

(c) Radial profile of gas-phase temperature

Fig. 11. Thin flame – spatial evolution; $p = 50$ atm, T_∞=1000 K, $Y_{F,MH} = 0.134$.

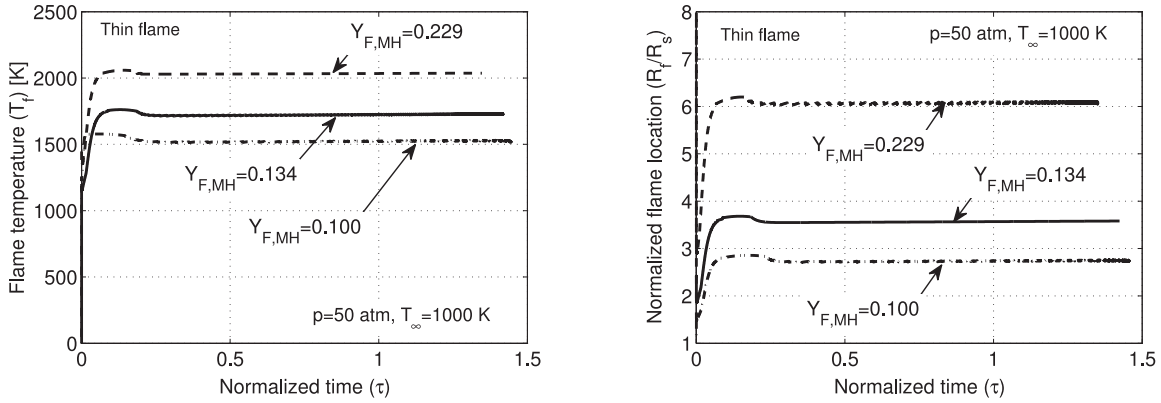

(a) Flame temperature (b) Flame location

Fig. 12. Thin flame – fuel content effect; p= 50 atm, T_∞=1000 K, $Y_{F,ls}$ = 0.1, 0.134, 0.229.

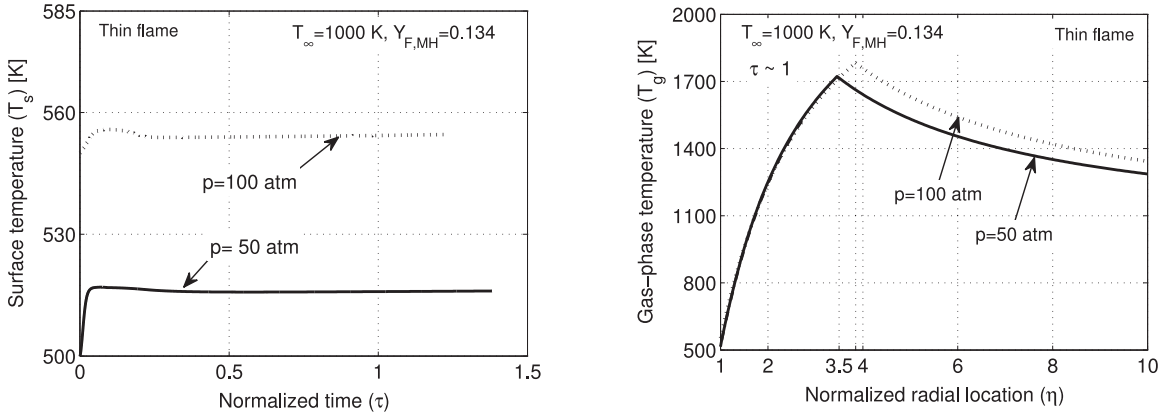

(a) Surface temperature (b) Flame location as a function of time

Fig. 13. Thin flame – ambient pressure effect; p = 50, 100 atm, T_∞ = 1000 K, $Y_{F,ls}$ = 0.134.

4.2.2. Ambient pressure effect

Again, higher ambient pressures imply higher wet-bulb temperatures, that trail higher surface temperatures (Fig. 13a). As a result higher flame temperatures are obtained (Fig. 13b). As expected, the maximal flame temperature is located farther away from the surface for 100 atm ($Rf/Rs \sim 3.9$) than for 50 atm ($Rf/Rs \sim 3.5$).

4.2.3. Ambient composition effect

If these hydrate particles burn in a gas environment heated by neighboring burning particles, higher fractions of water vapor and carbon-dioxide may prevail. As we can see, the presence of products in the environment means lower oxygen content and less heat production at the flame; thus, the flame temperature is reduced, as shown in Fig. 14a. As a result, the flame is nearer to the surface. The effect of the ambient water vapor is manifested also in the particle lifetime. As the quantity of the ambient water vapor is increased, the transport rates are decreased, prolonging particle lifetimes (Fig. 14b).

4.3. Radiation effect

Radiation effects are negligible both at low ambient temperatures ($T_\infty < 400$ K) and for small spheres ($R_s \leq 100$ μm). Thus, the solid curve in Fig. 15, representing simulation without (w/o) radiation and the dashed curve, represeting a 100-μm particle, are practically the same. For conditions at which radiation is important, two major issues should be addressed. First, the similarity of heat and mass transport (in Eqs. (2) and (6)) would be lost and Shvab–Zel'dovich variables could not be used. Second, these non-dimensional equations will no longer be size independent, and different calculations will be necessary for each initial radius. This implies that scaling changes; so, it will not be appropriate to scale times by the square of the original radius. Yet, if the presence of high water content, as for spray conditions that were mentioned in Section 4.2.3, causes an optically thick gas film, diffusion-like transport would result and the same scaling would be pertinent again.

The energy balance at the liquid–gas interface (Eq. (32)) would also have to address the radiative flux to and from the surface. Thus, for evaporation, the heat flux from the gaseous side would appear as follows:

$$\dot{q}_{g,s} = 4\pi R_s^2 \left(\lambda_g \frac{\partial T_g}{\partial r})_s + \sigma_B F (T_\infty^4 - T_s^4) \right) \tag{63}$$

where σ_B is Stefan–Boltzmann constant, ϵ is emissivity and F is shape factor.

The emissivity of water is close to 1 and, since we are dealing with an isolated sphere, then the shape factor should be equal to 1 as well ($F = 1$). Radiation shortens the lifetime of the particle and elevates the surface temperature.

For the thin-flame case, the radiation from the flame is larger than the radiation from the gas, since it is both hotter and closer to the sphere than the ambiance. Hence, T_∞ should be replaced with T_f.

The relative importance of the radiation flux $\dot{q}_{rad} \propto R_s^2 \sigma_B \epsilon_g F (T_\infty^4 - T_s^4)$ as compared with the conduction flux $\dot{q}_{cond} \propto R_s \lambda_g (T_\infty - T_s)$ is presented in Fig. 16a for evaporation, and in Fig. 16b for combustion (where T_∞, again, is replaced by T_f).

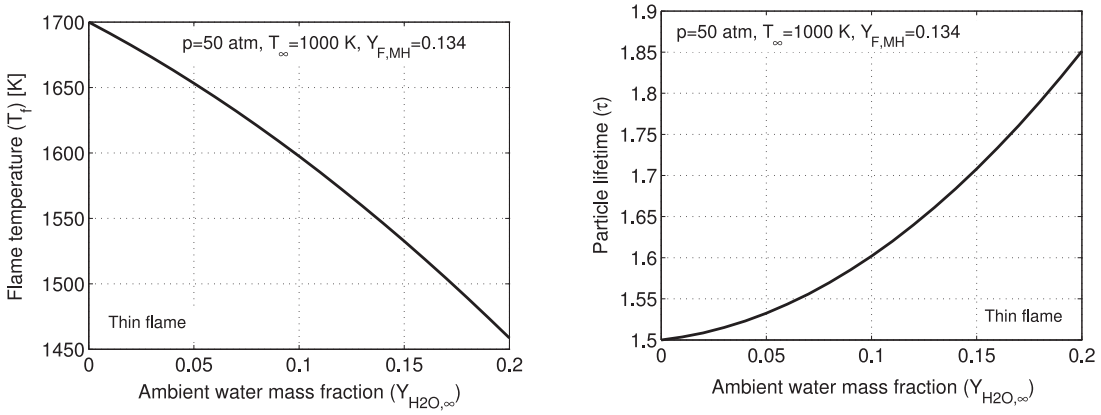

(a) Flame temperature (b) Particle lifetime

Fig. 14. Effect of ambient composition at nominal hydrate composition; $Y_{F,MH} = 0.134$, $p = 50$ atm, $T_\infty = 1000$ K.

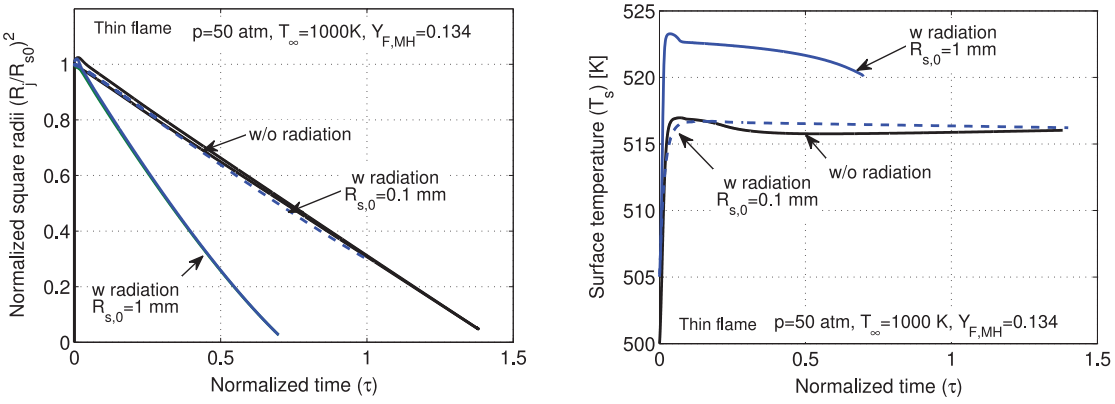

(a) History of hydrate radii (b) Surface temperature

Fig. 15. Radiation effects during evaporation of different size particles; $Y_{F,MH} = 0.134$, $p = 50$ atm, $T_\infty = 1000$ K.

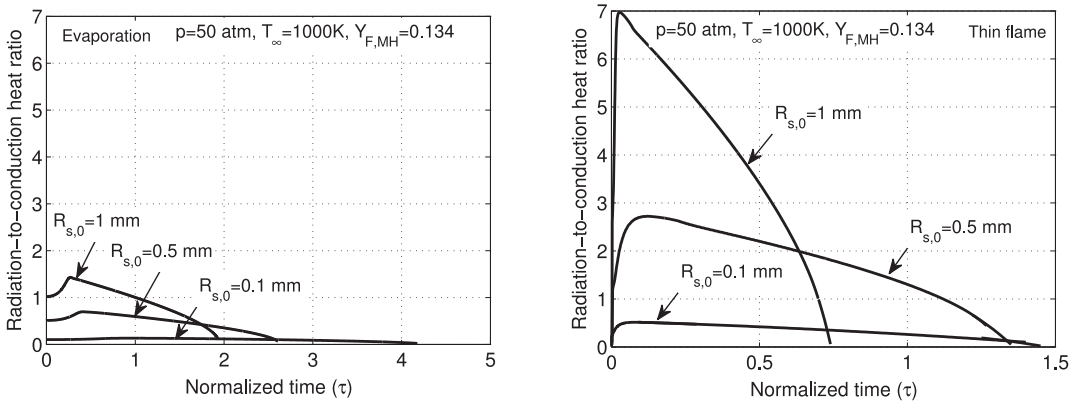

(a) Evaporation (b) Thin flame

Fig. 16. Heat flux ratio; $Y_{F,ls} = 0.134$ p =50 atm, $T_\infty = 1000$ K.

5. Summary and conclusions

Transient evaporation and combustion of methane hydrate were analyzed under the assumption of a diffusion-controlled process with a quasi-steady gas film in a spherically symmetric configuration. Buoyancy thermal radiation and drainage are neglected, considering only small spheres typical of pulverized fossil fuel. Diffusion-like transport prevails for low ambient temperatures and for small initial radius $R_S < 100$ μm, considering evaporation and combustion of small spheres. This could be the result of grinding bulks of methane hydrates, for example. Consequently, in this studied regime, the time development scales with the square of the initial particle radius.

The interest in high pressure burning is generated by three factors: greater thermal efficiency for power applications, greater stability of the hydrate, and opportunity for in situ combustion.

The non-dimensional temperature gradient through the bubbly mixture is not reaching a constant in time, nor is the ratio of the radii of the two surfaces. Quasi-steady behavior is not being reached asymptotically, in time. Thus, in spite of the behavior coming close to a linear variation for radius squared with time, that behavior is qualitatively different from the same result for the classical droplet. During the early portion of the evaporation period while the ice is still melting, the inner and outer boundaries of the bubbly mixture wrapping the solid core are both changing their sizes at different rates. The inner surface continuously recedes, while the outer surface first progresses due to the higher melting-to-vaporization flux ratio. As time develops, the bubbly mixture thickens and more heat is conducted into it, leading to an inversion in the melting-to-evaporation flux ratio, and to the receding of both interfaces, yet at continuously decreasing ratio.

When all hydrate cavities are filled, the ratio of water-to-methane molecules is 5.75 ($Y_{F,MH} = 0.134$). The methane-water bonds are broken upon melting. Negligible methane dissolves in the liquid water due to low Henry's law constants. At high pressures, the methane bubbles are expected to be small and flow with the water within the bubbly mixture.

The driving force of the evaporation and combustion processes is the heat flux at the droplet surface from the surrounding flame or hot ambient air. Therefore, lowering the ambient temperature or reducing the fuel content in the hydrate reduces mass flow rates. Lower methane content (i.e., higher water content) results in lower flame temperatures; thus, the flame is located closer to the surface of the droplet. With lower fuel content in the hydrate, both the water vaporization rate and fuel burning rate are lowered. For hydrate particles burning in the presence of other burning particles, higher fractions of products will prevail. The water, in particular, will serve as a heat sink and will cause lower flame and surface temperatures.

Many interesting issues remain for future study. As particle size is increased, various gravity-related issues must be addressed including buoyancy of the heated gases in the flame, drainage or dripping of the melted ice, and migration of methane bubbles through the liquid. Moreover, thermal radiation would no longer be negligible. Clearly, spherical symmetry would be destroyed, and scaling rules would change. Even without gravity effects, larger bubbles could migrate randomly and reach the outer interface. More sophisticated chemical kinetic schemes should be used to study ignition and/or pollutant formation. If very high pressures occur, important effects of near-critical thermodynamic behavior must be examined: e.g., modification of phase equilibrium rules and energy of vaporization. Combustion at high pressure is thermodynamically efficient and produces high levels of power. Although there is currently no clear technology for an in-situ high pressure combustion of methane hydrates, it is vital to analyze the opportunities. Finally, practical, high mass flow configurations will require analyses that consider dense sprays and relative motion between the hydrate particle and the oxidizing gas.

Acknowledgments

We value interesting discussions with Professors D. Dunn-Rankin and P. Taborek about background material and their preliminary experimental results. Support from NSF Grant CBET-1333605 with Dr. Ruey-Hung Chen as Program Manager is greatly appreciated.

Appendix

Table 1
Thermophysical properties.

Property	Value/equation	Ref. remark
C_{p,g,CH_4}	3.31	$\frac{J}{gcc}$ [26]
ρ_{MH}	0.912	$\frac{g}{cc}$ [3]–[23]
ρ_{ice}	0.916	$\frac{g}{cc}$ [a]
L_{melt}	334	$\frac{J}{g}$ [a]
L_{vap}	$0.0164p^4 - 0.7231p^3 + 11.49p^2 - 140.53p + 2133.2p$ [MPa]	$\frac{J}{g}$ [a]
C_{p,L,H_2O}	p=5 MPa and $T <$ 374 K$\rightarrow 1.35e-5T_L^2 - 0.0086T_L + 5.5425$ p=5 MPa and $T < T_{sat} \rightarrow 3.3e-5T_L^2 - 0.0254T_L + 9.1107$	$\frac{J}{gK}$ [a]
λ_{L,H_2O}	$-5.6e-6T_L^2 + 0.0047T_L - 0.292$	$\frac{J}{gK}$ [a]
ρ_{H_2O}	$-3.81e-5T_L^4 + 0.062T_L^3 - 39.672T_L^2 + 10,903T_L - 67,600$	$\frac{g}{cc}$ [a]

[a] http://webbook.nist.gov/chemistry/fluid/.

References

[1] E. D. Sloan Jr., C. Koh, Clathrate hydrates of natural gases, 2007, CRC Press.
[2] C. Ruppel, Methane hydrates and the future of natural gas, MITEI natural gas report, Suppl. Pap. Methane Hydrates 4 (2011) 25.
[3] M. Max, Natural gas hydrate in oceanic and permafrost environments, vol. 5, Springer, 2003.
[4] A. Demirbas, Methane hydrates as potential energy resource: Part 2–methane production processes from gas hydrates, Energy Convers. Manag. 51 (7) (2010) 1562–1571.
[5] C. Cranganu, In-situ thermal stimulation of gas hydrates, J. Pet. Sci. Eng. 65 (1) (2009) 76–80.
[6] W.C. Pfefferle by dissociating methane hydrate deposits in-situ wherein an oxidizer fluid and a supply of fuel, both at a pressure higher than that of the methane hydrate deposit are delivered downhole and combusted, with heat of reaction dissociating the methane. Method of natural gas production. US Patent no. 6973968, 2005.
[7] E.D. Sloan, Fundamental principles and applications of natural gas hydrates, Nature 426 (2003) 353–363.
[8] V.E. Nakroyakov, S.Y. Misyura, S.L. Elistratov, A.Y. Manakov, A.A. Sizikov, Methane combustion in hydrate systems: water-methane and water-methane-isopropanol, J. Eng. Thermophys. 22 (2013) 169–173.
[9] M. Roshandell, J. Glassman, M. Khalil, P. Taborek, D. Dunn-Rankin, Burning ice – direct combustion of fuel clathrates, in: Proceedings of the 7th US National Combustion Meeting, 2011.
[10] U.S. Department of Energy, Annual Energy Utlook 2013 With Projections to 2040. Report No. DOE/EIA-0383(2013), DOE, 2013 http://www.eia.gov/forecasts/aeo/pdf/0383(2013).pdf.
[11] C.D. Rokosh, J.G. Pawlowicz, H. Berhane, S.D.A. Anderson, A.P. Beaton, What is Shale Gas? An Introduction to Shale-gas Geology in Alberta, ERCB/AGS Open File Report, 2008-08, Energy Resources Conservation Board, Alberta Geological Survey, 2008.
[12] S.G. Osborn, A. Vengosh, N.R. Warner, R.B. Jackson, Methane contamination of drinking water accompanying gas-well drilling and hydraulic fracturing, Proc. Natl. Acad. Sci. USA 108 (2011) 8172–8176, doi:10.1073/pnas.1100682108.
[13] W.A. Sirignano, Fluid dynamics and transport of droplets and sprays, second edition, Cambridge University Press, 2010.
[14] S. Sazhin, Advanced models of fuel droplet heating and evaporation, Prog. Energy Combust. Sci. 32 (2006) 162–214.
[15] C.K. Law, Recent advances in droplet vaporization and combustion, Prog. Energy Combust. Sci. 8 (1982) 171–201.
[16] Y.C. Liu, T. Farouk, A.J. Savas, F.L. Dryer, C. Thomas Avedisian, On the spherically symmetrical combustion of methyl decanoate droplets and comparisons with detailed numerical modeling, Combust. Flame 160 (2013) 641–655.
[17] S. Kirby, L.A. Stern, S. Circone, W. Durham, Anomalous preservation of pure methane hydrate at 1 atm, J. Phys. Chem. B 105 (9) (2001) 1756–1762.
[18] O. Konrad, T. Lankau, The significance of the methane water interaction potential, J. Phys. Chem. 109 (2005) 23596–23604.
[19] D.R. Lide, CRC handbook of chemistry and physics, CRC Press, 2004.
[20] F.A. Williams, Combustion theory: The fundamental theory of chemical reacting flow systems, Addison-Wesley, 1965.

[21] W.F. Waite, L.A. Stern, S. Kirby, W.J. Winters, D. Mason, Simultaneous determination of thermal conductivity, thermal diffusivity and specific heat in si methane hydrate, Geophys. J. Int. 169 (2) (2007) 767–774.
[22] E.J. Rosenbaum, N.J. English, J.K. Johnson, D.W. Shaw, R.P. Warzinski, Thermal conductivity of methane hydrate from experiment and molecular simulation, J. Phys. Chem. B 111 (46) (2007) 13194–13205.
[23] Y. Handa, D. Stupin, Thermodynamic properties and dissociation characteristics of methane and propane hydrates in 70-. ang.-radius silica gel pores, J. Phys. Chem. 96 (21) (1992) 8599–8603.
[24] F.E. Fendell, M.L. Sprankle, D.S. Dowson, Thin-flame theory for a fuel droplet in slow viscous flow, J. Fluid Mech. 26 (2) (1966) 267–280.
[25] C. Robinson, D.B. Smith, The auto-ignition temperature of methane, J. Hazard. Mater. 8 (3) (1984) 199–203.
[26] ASTM D3956-12: Standard Specification for Methane Thermophysical Property Tables, ASTM 3956-12, ASTM International, 2012.